KONA Powder and Particle Journal No. 38 (2021) 168–188/https://doi.org/10.14356/kona.2021003 Review Paper

Coal Particle Devolatilization and Soot Formation in Pulverized Coal Combustion Fields †

Nozomu Hashimoto [1]* and Jun Hayashi [2]

[1] *Division of Mechanical and Space Engineering, Hokkaido University, Japan*
[2] *Department of Energy Conversion Science, Kyoto University, Japan*

Abstract

In this paper, recent developments of the devolatilization model and soot-formation model for the numerical simulations of pulverized-coal combustion fields, and the technology used to measure soot particles in pulverized-coal combustion fields are reviewed. For the development of new models, the validation of the developed models using measurement is necessary to check the accuracy of the models because new models without validation have a possibility to make large errors in simulations. We have developed the tabulated devolatilization process model (TDP model) that can take into account the effect of particle heating rate on the volatile matter amount and the devolatilization-rate parameters. The accuracy of the developed TDP model was validated by using the laser Doppler velocimetry data for the bench-scale coal combustion test furnace. The soot-formation model combined with TDP model for the large eddy simulation (LES) has been also developed. The spatial distributions of both the soot-volume fraction and the polycyclic aromatic hydrocarbons were measured by virtue of laser-induced incandescence (LII) and laser-induced chemiluminescence (PAHs-LIF). The accuracy of the developed soot-formation model was validated by using the measured data.

Keywords: coal combustion, soot, devolatilization, numerical simulation, optical diagnostics, laser induced incandescence

1. Introduction

Pulverized coal combustion has been introduced to many coal-fired thermal power plants across the world. However, since the CO_2 emissions from coal-fired thermal power plants is larger than that from other power plants, efficient operation of these power plants and introducing new types of fuel that can be produced from renewable energy is expected. To realize that, modifications of coal-fired thermal power plants are needed. Because the cost of modifying large-scale power plants would be large, pre-evaluation of the modifications is necessary. Numerical simulation of pulverized coal combustion field can be a powerful tool for such pre-evaluation of the modifications or improvement of the operation for the coal-fired thermal power plants. The research group of the authors have conducted studies relating to the development of numerical simulation technology for coal combustion fields (Hashimoto N. et al., 2007, 2012a, 2012b, 2014, 2016b, 2017; Kurose R. et al., 2003, 2004, 2007, 2009; Watanabe H. et al., 2009; Muto M. et al., 2015; Ahn S. et al., 2017).

Fig. 1 illustrates an example of the prediction results of a coal particle's temperature in an actual large-scale coal-fired boiler by the developed numerical simulation technology for coal combustion fields. **Fig. 2** illustrates the calculated O_2 concentration distribution on the furnace wall surface and the comparison of measured and calculated O_2 concentrations at the inspection windows on the furnace wall for the same boiler as in **Fig. 1**. The circled numbers in **Fig. 2(a)** indicate the locations of the inspection windows. Indeed, the simulation suggests that the O_2 concentration at the inspection window at the rear side all above the burner zone (② in **Fig. 2(b)**) is low compared to the front side wall. However, discrepancies exist between the simulation results and the measured data. Accordingly, room for improvement with respect to the accuracy of the numerical simulation exists, which can be achieved by understanding the processes involved in pulverized coal combustion fields.

Fig. 3 shows the basic concept of the pulverized coal combustion process. When the pulverized coal particle is heated up, moisture evaporates from the particle at the

† Received 21 October 2019; Accepted 15 January 2020
J-STAGE Advance published online 31 March 2020
[1] Kita 13 Nishi 8, Kita-ku, Sapporo 060-8628, Japan
[2] Yoshidahonmachi, Sakyo-ku, Kyoto 606-8501, Japan
* Corresponding author: Nozomu Hashimoto;
E-mail: nozomu.hashimoto@eng.hokudai.ac.jp
TEL: +81-11-706-6386

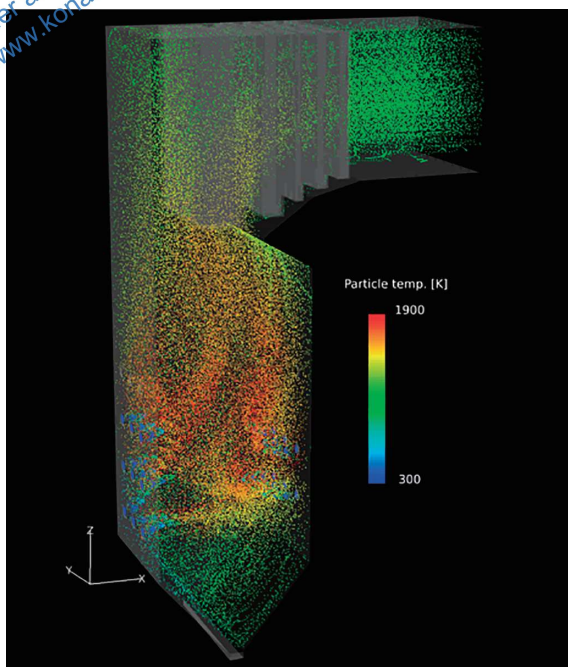

Fig. 1 Prediction of coal particle's temperature in actual 915 MW_{th} class boiler.

temperature range of boiling point of water. The volatile matter, which includes various gas species and tar, evolves from the particle by the devolatilization process: the gaseous fuels are rapidly oxidized by oxygen in a combustion field. Indeed, it is well known that the majority of the tar is converted into soot particles in the secondary pyrolysis-reaction process. The soot particle emits strong radiation same as the char particle. In addition, the oxidation process of soot particles is relatively slow compared to that of gaseous fuel species. The char combustion process after coal-particle devolatilization has been studied by many researchers across the world. This is because unburned carbon in fly ash that is captured from the exhaust gas is the major concern in the coal combustion research field. Therefore, the researches on the devolatilization and soot formation processes in coal combustion field have been limited. However, the devolatilization process and the soot formation process is very important for the numerical simulation of coal combustion field, because the treatment of these processes strongly affects the prediction accuracy of the entire oxidation speed of the volatile matter and temperature field of the burner zone.

The research group of the authors have conducted studies concerning two major elements: (i) developing the devolatilization and soot-formation models for numerical simulations of the coal combustion fields and (ii) measuring the soot particles present in the coal combustion fields by using optical-diagnostic systems equipped with high power lasers. In this paper, recent attempts to develop accurate numerical simulation technology for coal combustion field are reviewed.

2. Coal-particle devolatilization

Coal-particle devolatilization is a crucial phenomenon in the entire coal combustion process. Volatile matter evolves from coal particles during the devolatilization process. Indeed, both the devolatilization rate and the volatile-matter amount affect the coal-combustion process significantly. In this chapter, the models for the prediction of the devolatilization process are reviewed, as well as methods that aim to unite the devolatilization process model and the numerical simulation of coal combustion fields.

2.1 Models for devolatilization of coal particles

Several devolatilization models have been developed by many researchers, such as the CPD model by Fletcher T.H. et al. (1990), FG-DVC model by Solomon P.R. et al. (1988), and FLASHCHAIN model by Niksa S. and Kerstein A.R. (1991). In the CPD model, percolation-lattice statistics are employed in order to describe the generation of tar precursors of finite size based on the number of cleaved labile bonds in the infinite coal lattice. The FG-DVC model combines a functional-group model for gas evolution and a statistical model for tar formation, including depolymerization, cross-linking, external transport and internal transport. Finally, in the FLASHCHAIN model, the chemical constitution of coal in terms of typical refractory aromatic nucleus, two linkage types (labile bridges and char links), and a typical peripheral group are rendered, the labile bridges are regarded as the key reaction centers.

The following formula, which was proposed by Badzioch and Hawksley (1970), is commonly used in modeling the devolatilization process with respect to numerically simulating coal-combustion fields:

$$\frac{\mathrm{d}V}{\mathrm{d}t} = K_{\mathrm{v}}(V^{*} - V) \tag{1}$$

$$K_{\mathrm{v}} = A_{\mathrm{v}} \exp\left(-\frac{E_{\mathrm{v}}}{RT_{\mathrm{p}}}\right) \tag{2}$$

where, V represents the mass of volatile matter that evolved from a coal particle (kg), V^{*} represents the mass of volatile matter in particle (kg), A_{v} represents the pre-exponential factor for the volatile-matter evolution-rate equation (1/s), E_{v} represents the activation energy for the volatile-matter evolution-rate equation (J/kmol), R represents the gas constant (J/(mol K)), and T_{p} represents the particle temperature (K).

$$V^{*} = QV^{*\prime} \tag{3}$$

where $V^{*\prime}$ and Q are, respectively, the amount of volatile

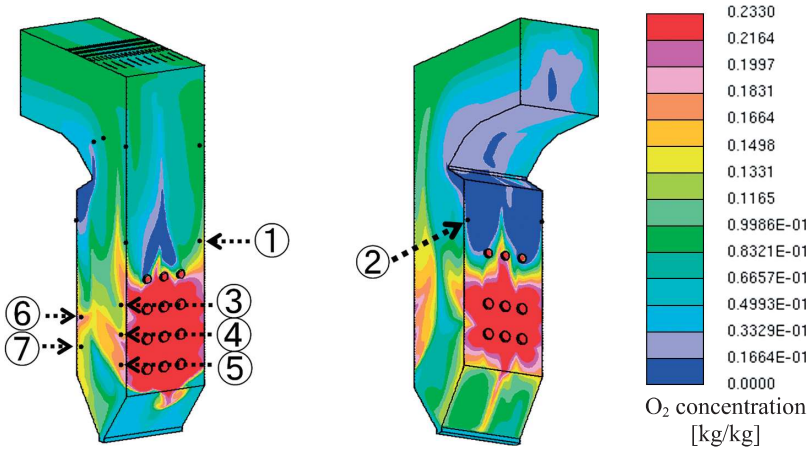

(a) Calculated O_2 concentration on furnace wall surface and positions of inspection windows

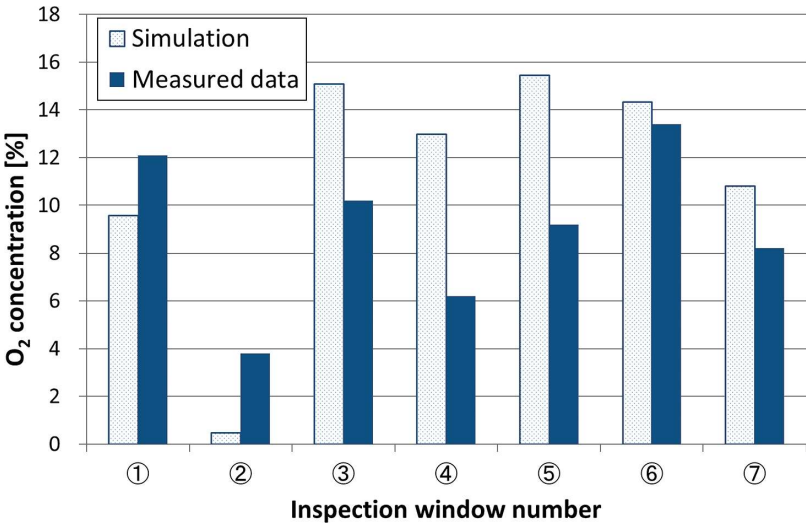

(b) O_2 concentration at inspection windows

Fig. 2 Comparison of measured and calculated O_2 concentrations at inspection windows on furnace wall surface for the 915 MW_{th} boiler. Reprinted with permission from Ref. (Hashimoto N. and Watanabe H., 2016b). Copyright: (2016) Elsevier B.V.

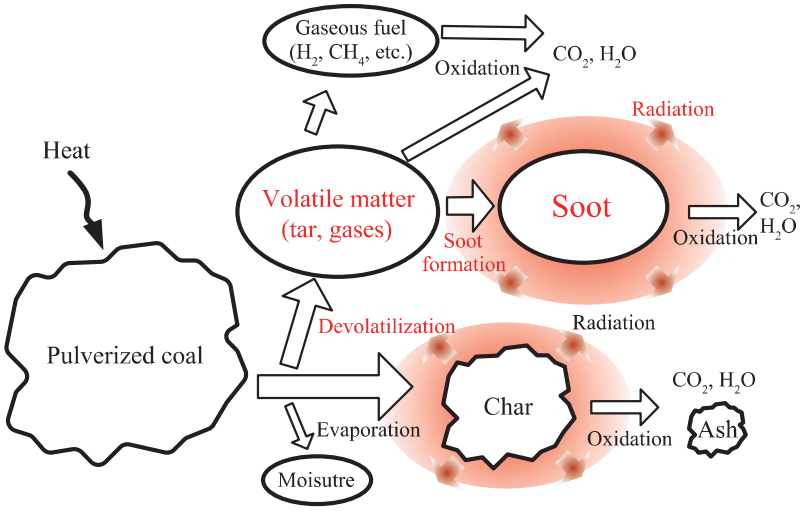

Fig. 3 Basic concept of pulverized combustion process.

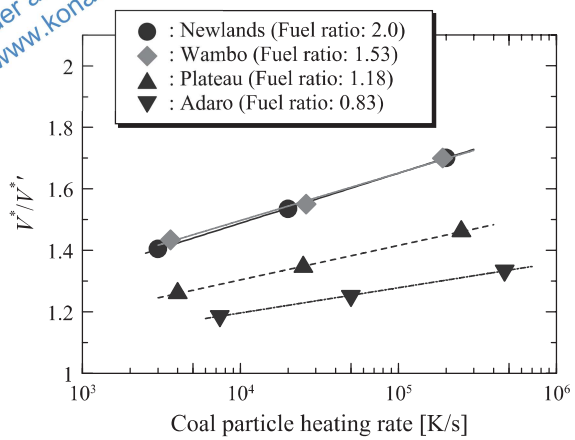

Fig. 4 *V*/V*'* (Appropriate value for Q-factor) as a function of the coal particle heating rate calculated by FLASHCHAIN model. Reprinted with permission from Ref. (Hashimoto N. et al., 2012a). Copyright: (2012) Elsevier B.V.

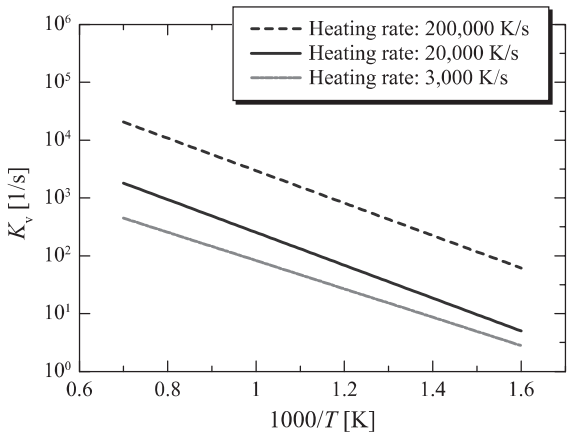

Fig. 5 Effect of the coal particle heating rate on K_v (in Eq. (1)) for Newlands bituminous coal calculated by the FLASHCHAIN model. Reprinted with permission from Ref. (Hashimoto N. et al., 2012a). Copyright: (2012) Elsevier B.V.

matter obtained by proximate analysis and the Q-factor, the latter of which is employed in order to identify the rate at which the amount of volatile matter increases according to the high particle-heating rate in pulverized-coal combustion fields. In the conventional model for numerical simulations of coal combustion, A_v, E_v and Q are treated as constant values for all coal particles regardless of the particle-heating rate. However, the value of V^* is dependent on the coal particle-heating rate. Therefore, appropriate values for A_v, E_v, and Q are significantly affected by the diameter of each particle, as well as how each particle is injected to the coal-combustion field. Indeed, such effects are not considered in the conventional model.

To investigate the effects of the coal-particle heating rate on A_v, E_v and $V^*/V^{*\prime}$, the FLASHCHAIN model was used to conduct devolatilization simulations. **Fig. 4** shows $V^*/V^{*\prime}$, which represents appropriate values for the Q-factor as a function of the particle-heating rate for different coal brands. **Fig. 5** shows the effect of the particle-heating rate on the devolatilization-rate coefficient, K_v, for Newlands' bituminous coal, which was predicted using the FLASHCHAIN model. From these figures, it is evident that both the volatile-matter amount and the devolatilization rate are significantly affected by the particle-heating rate. We developed a new model to consider this significant effect of the particle-heating rate on the volatile-matter amount and the devolatilization-rate parameters, the details of which are reviewed in the next section.

2.2 Tabulated devolatilization process model

To consider the variation of the devolatilization rate and the volatile matter amount for each coal particle in the numerical simulation, the tabulated-devolatilization-process (TDP) model was developed. In the TDP model, suitable values for the devolatilization parameters are automatically set for each coal particle according to the procedure outlined below for a steady-state calculation.

1. The devolatilization parameters are set at initial values (① in **Fig. 6**).
2. An iteration of the CFD calculation is carried out using the devolatilization parameters (② in **Fig. 6**).
3. After the iteration, the particle temperature history of each coal particle calculated in the most recent CFD iteration is compared with the temperature histories in the devolatilization database. The temperature history from the data base that is closest to the particle temperature history calculated from the most recent CFD iteration is selected (③ in **Fig. 6**).
4. The devolatilization parameters accompanied with the extracted temperature history are used in the next CFD iteration (④ in **Fig. 6**).

Steps 2–4 are repeated until the CFD calculation converges. The procedure mentioned above is for the steady state simulation. The procedure for unsteady simulations such as the large eddy simulation (LES), will be reviewed in **Section 4**.

In the TDP model, the mass fraction of volatile matter in the particle m_{vola} (kg/kg-coal) changes depending on the particle-heating rate. Indeed, variations in m_{vola} imply variations in the volatile matter calorific value and the chemical-element composition balance. Therefore, the mole fractions of the postulated chemical species as volatile matter vary depending on the value of m_{vola}. This result means that the calorific value and the elemental-component balance of the volatile matter varies depending of the particle-heating rate. The detailed procedure used to conform both the calorific value and elemental component balance of a coal particle in the numerical simulation to the calorific value obtained by both proximate analysis and ultimate analysis is available in the relevant literatures: Hashimoto N. et al. (2012a, 2012b), and Hashimoto N. and Shirai H. (2014).

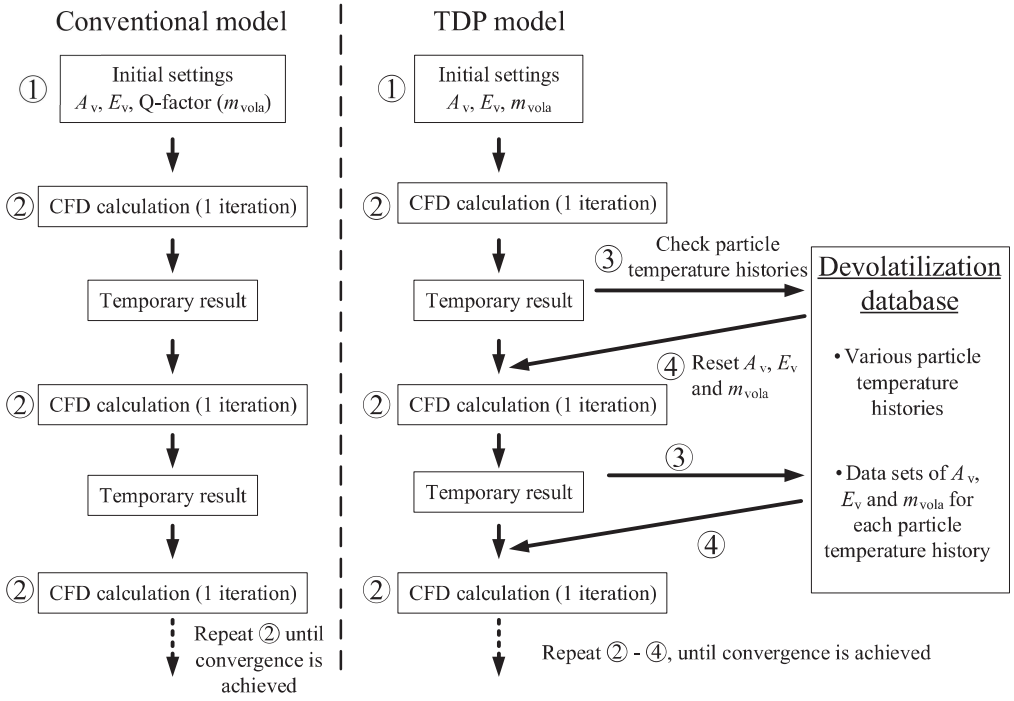

Fig. 6 Calculation flow chart of the TDP model for steady state numerical simulation. Reprinted with permission from Ref. (Hashimoto N. et al., 2012a). Copyright: (2012) Elsevier B.V.

The validation of the model was conducted using the optical measurement data of the 760 kW_{th} coal-combustion test furnace (**Fig. 7**). A laser Doppler velocimetry (LDV) was employed to obtain the particle-velocity distributions in the test furnace. **Fig. 8** shows a schematic of the measurement system.

Fig. 9 shows the comparison of radial distributions of mean axial-particle velocities. Case 1 indicates the particle velocity predicted by the TDP model. Cases 2–4 indicate the particle velocities predicted by the conventional model. The devolatilization rate parameters used for the conventional model are listed in **Table 1**. Cases 5–7 indicate the particle velocities predicted by the two competing reaction-rate model (Kobayashi et al., 1977). The devolatilization-rate parameters for the two competing reaction rate model are listed in **Table 2**. In **Fig. 9**, the mean axial velocity, U_z, for the Case 1 (TDP model) is more agreeable with the LDV results compared to other cases, which tend to underestimate the values of U_z around the central axis. From the above results, it is clear that the TDP model (Case 1) is better at reproducing the coal-combustion experiment than the other models.

Fig. 10 shows the selection probability of temperature histories in the devolatilization database, when the particle-temperature histories calculated in the CFD iteration are compared with the temperature histories in the database (**Fig. 6**). Indeed, for the majority of particles, the heating rate is in the range of 10^4–10^6 K/s. Moreover, large variations in the particle-heating rate exist according to the initial diameter as shown in **Fig. 10**: the smaller the initial diameter is, the higher the particle heating rate is. This result indicates that the particle-heating rate should be considered for all coal particles in the field, because it is affected by particle diameter and the position at which said particle is injected into the combustion field. Therefore, devolatilization models that consider the effect of the particle-heating rate on the devolatilization characteristics, such as the TDP model, are strongly recommended for the numerical simulations of pulverized-coal combustion fields.

3. Soot formation in pulverized coal combustion field

As discussed in Chapter 1, the majority of tar that evolves from a coal particle is converted into soot particles as a consequence of secondary pyrolysis. These soot particles emit the strong radiation same as the char particles. Therefore, accurate models with respect to the formation of soot particles can improve predictions about temperature distribution in pulverized-coal combustion fields. Unfortunately, soot formation in pulverized coal flames is yet to be fully understood. In this chapter, experimental research concerned with employing the optical diagnostics of soot particles for coal combustion fields are reviewed as well as research concerning the development of soot-formation models for the LES of coal-combustion fields. For the purposes of validation, the spatial distribution of the soot-volume fraction, which can be obtained by employing a strong pulse laser is one of the most valuable data.

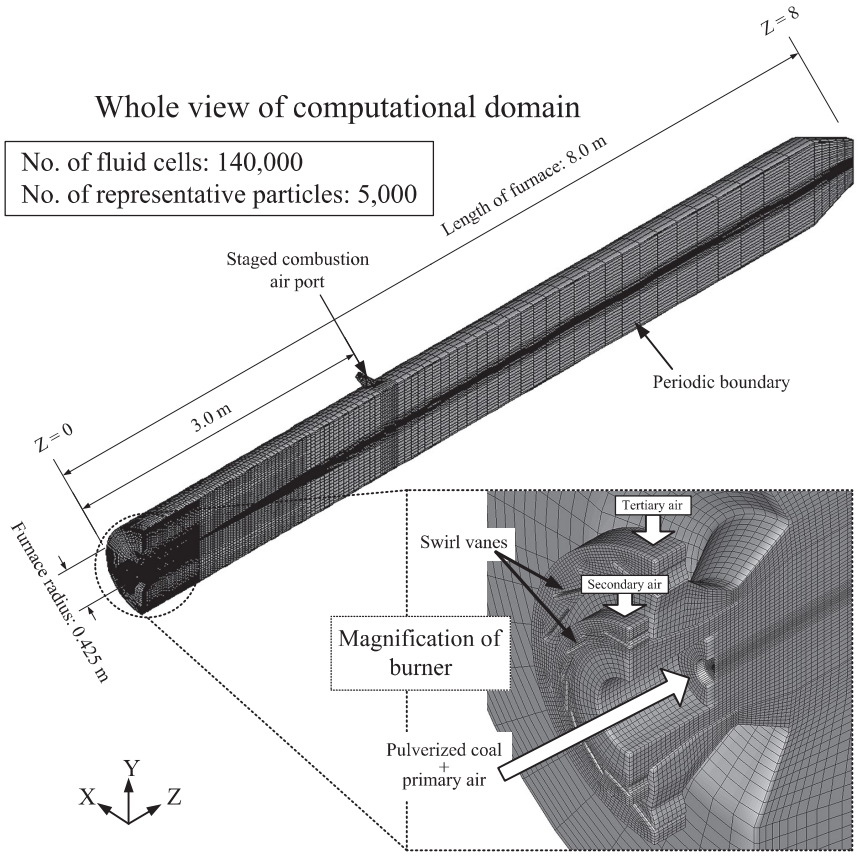

Fig. 7 Computational domain for the validation of the TDP model for steady state simulation. Reprinted with permission from Ref. (Hashimoto N. et al., 2012a). Copyright: (2012) Elsevier B.V.

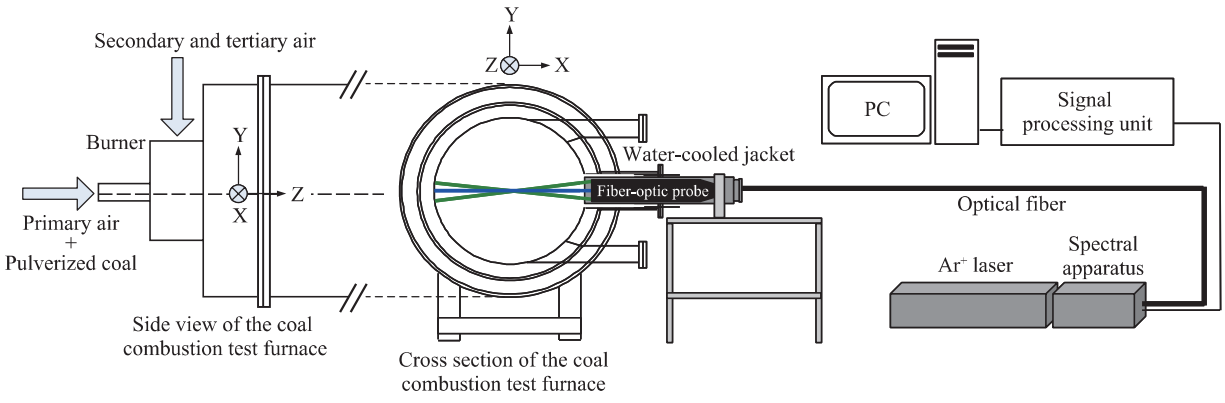

Fig. 8 Schematic illustration of laser Doppler velocimetry for the 760 kW_{th} coal combustion test furnace. Reprinted with permission from Ref. (Hashimoto N. et al., 2012a). Copyright: (2012) Elsevier B.V.

Table 1 Parameters for the conventional model. Reprinted with permission from Ref. (Hashimoto N. et al., 2012a). Copyright: (2012) Elsevier B.V.

Case	Ref.	A_v [1/s]	E_v [J/kmol]	Q [-]
2	Tominaga et al., 1997	2.02×10^3	3.11×10^7	1.2
3	Solomon et al., 1983	4.5×10^{13}	2.20×10^8	1.5
4	Johnson et al., 1988	1.0×10^{13}	1.8×10^8	1.8

3.1 Pulverized-coal jet flame burner and the conditions for non-intrusive soot diagnostics

To obtain precise soot formation data with respect to pulverized-coal flames, a simple co-axial pulverized-coal jet burner in CRIEPI (Hwang S.M. et al., 2005) was selected. The coal jet burner and the supplying system are illustrated in **Fig. 11**. Pulverized coal particles and air were supplied to a combustion field from the main burner port (diameter: 6 mm) as the “premixed coal/air flow”. Methane was issued from a slit with a width of 0.5 mm

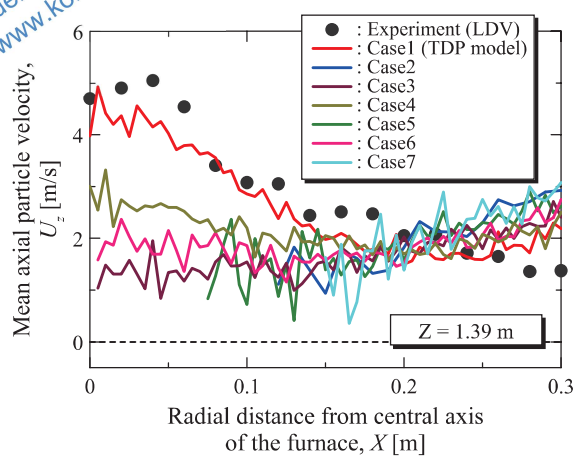

Fig. 9 Radial distributions of average axial particle velocities. Reprinted with permission from Ref. (Hashimoto N. et al., 2012a). Copyright: (2012) Elsevier B.V.

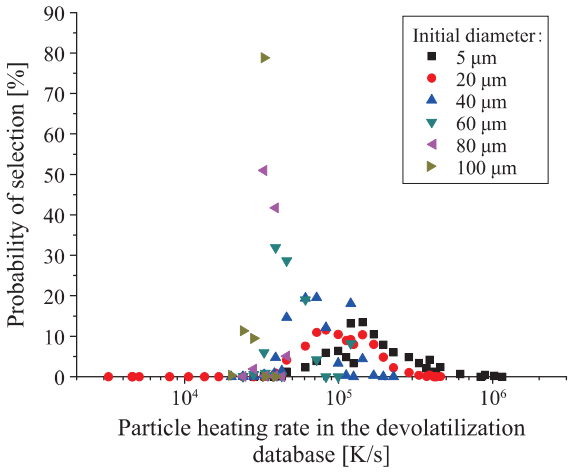

Fig. 10 Probability of selection for heating rate in the devolatilization database during the extraction process. Reprinted with permission from Ref. (Hashimoto N. et al., 2012a). Copyright: (2012) Elsevier B.V.

Table 2 Parameters used for the two competing reaction rate models. Reprinted with permission from Ref. (Hashimoto N. et al., 2012a). Copyright: (2012) Elsevier B.V.

Case	Ref.	α_1	α_2	A_1 [1/s]	A_2 [1/s]	E_1 [J/kmol]	E_2 [J/kmol]
5	Kobayashi et al., 1977	0.3	1	2.0×10^5	1.3×10^7	1.05×10^8	1.67×10^8
6	Cho et al., 2007	0.38	0.8	3.7×10^5	1.46×10^{13}	7.4×10^7	2.5×10^8
7	Ubhayakar et al., 1976	0.292	0.438	3.7×10^5	1.46×10^{13}	7.4×10^7	2.5×10^8

that was placed outside the main burner port, in order to stabilize the pulverized-coal flame.

Tables 3 and **4** show the properties of coal and the conditions for pulverized coal flame, respectively. Newlands bituminous coal was selected as the fuel. The mass-based median diameter measured by a laser diffraction particle size analyzer was 33 μm, and the number-based average diameter was 25 μm. The air/coal mass ratio was set to 1.58.

3.2 Preparation of the laser-induced incandescence (LII) in the pulverized-coal flame

Although the laser induced incandescence (LII) is a non-intrusive diagnostic that obtains the volume fraction of primary soot particles in the flame (Michelsen H.A., 2017), both the laser-sheet profile and the laser-pulse fluence should be carefully adjusted when applying LII to the pulverized-coal flame.

Fig. 12 shows the cross section of the laser-intensity profile at the center of the measurement plane (the center of the main burner port). A thin laser sheet was shaped by four cylindrical lenses with focus lengths of $f = -300$ mm, 25 mm, 700 mm, and 2,000 mm. (Note that this optical setup was same in all experiments in this chapter). The laser sheet has the Gaussian profile in the horizontal axis, as shown in **Fig. 12**. The laser sheet thickness was defined by taking $1/e^2$ of the maximum intensity. The LII signals obtained by the Gaussian profile (full sheet) and the homogeneous profile (partial sheet) were examined by Hayashi J. et al. (2013), in order to understand the effects of the laser profiles on the LII applied to the pulverized-coal flame.

The relation between the signal intensity of the LII and the laser-pulse fluences are shown in **Fig. 13**. The values in **Fig. 13** were normalized using the signal intensity of the LII at a laser fluence of 0.1 J/cm^2. Results obtained in the non-combustion case were normalized by the signal intensity of the LII in the Gaussian profile at the same laser fluence as other combustion cases. Indeed, from **Fig. 13**, it is evident that three regions in the combustion case exist: the heating region **(a)**, the plateau region **(b)**, and the superimposed region **(c)**. In region **(a)**, the signal intensity of the LII increases with an increase in the laser fluence. In this region, the laser fluence is insufficient with respect to heating all the soot particles in the measurement area up to the sublimation temperature. In region **(b)**, the signal intensity of the LII decreases slightly with an increase in the laser fluence, ultimately plateauing. Indeed, these two regions—**(a)** and **(b)**—can also be found in the LII measurements of gaseous flames (Schulz C. et al., 2006). For gaseous and spray (Hayashi J. et al., 2011) flames, LII was conducted with the laser fluence in this plateau region. This is because the signal intensity of the LII does not change with an attenuation of the measurement field. However, to apply LII to the context of a pulverized-coal flame, the laser fluence should be care-

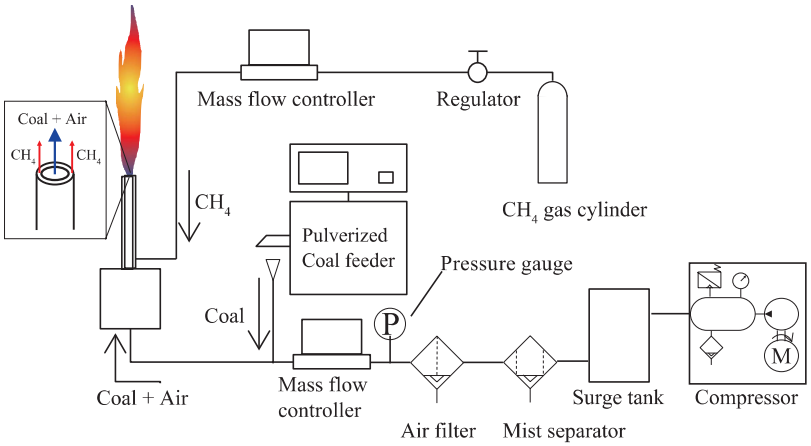

Fig. 11 Schematic of the coal jet burner and supplying system. Reprinted with permission from Ref. (Hayashi J. et al., 2019). Copyright: (2019) Elsevier B.V.

Table 3 Properties of coal. Reprinted with permission from Ref. (Hayashi J. et al., 2013). Copyright: (2013) Elsevier B.V.

Item	Value
Higher heating value[a]	29.1 MJ/kg
Lower heating value[a]	28.1 MJ/kg
Proximate analysis	
Moisture[b]	2.60 wt%
Ash[a]	15.20 wt%
Volatile matter[a]	26.90 wt%
Fixed carbon[a]	57.90 wt%
Ultimate analysis	
Carbon[a]	71.90 wt%
Hydrogen[a]	4.40 wt%
Nitrogen[a]	1.50 wt%
Oxygen[a]	6.53 wt%
Total sulfur[a]	0.44 wt%
Combustible sulfur[a]	0.39 wt%

[a] Dry basis, [b] As received

Table 4 Experimental conditions. Reprinted with permission from Ref. (Hayashi J. et al., 2013). Copyright: (2013) Elsevier B.V.

Item	Value
Pulverized coal feed rate	1.49×10^{-4} kg/s
Thermal input of coal[a]	4.19 kW
Thermal input of CH_4[a]	0.83 kW
Air flow rate	1.80×10^{-4} m^3/s
CH_4 flow rate	2.33×10^{-5} m^3/s
Bulk equivalence ratio	$\phi = 6.09$
Reynolds number, *Re*	2,544

[a] Based on the lower heating value

fully controlled according to region **(c)**. While region **(c)** is evident in pulverized-coal flames, it does not appear in the LII measurements for the flames of both gaseous and liquid fuels. As shown in region **(c)** of **Fig. 13**, the signal intensity of the LII re-increases with an increase in the laser fluence. This result is because the signals of the LII from the pulverized-coal particles are superimposed onto the signals of the LII from the soot particles. Indeed, the LII signal in the non-combustion case, in which there are no soot formation, increases in the range of laser fluence with higher than 0.2 J/cm^2 (shown as the solid square in **Fig. 13**).

These results suggest that sufficient fluence of the laser is required to heat all the soot particles up to the sublimation temperature so that all the soot particles emit enough LII signals for the evaluation of the soot particle volume fraction in pulverized coal flames. At the same time, it should be mentioned that too high fluence of laser may cause the overestimation of the volume fraction of soot particles in pulverized coal flame due to the signals of LII from the pulverized coal particles.

3.3 Simultaneous measurements of LII and Mie scattering, and comparisons with OH-PLIF

In this section, the simultaneous measurements of Mie scattering and the LII in the pulverized coal flame are discussed in order to understand how the coal particles and soot formation are related. Two-dimensional images of Mie scattering and the LII with OH-PLIF (Hwang S.M. et al., 2005) are shown in **Fig. 14**, from which it is evident that the signals of Mie scattering are strong near the burner port and it decreases with an increase in height above the burner port (HAB). Contrastingly, the LII and the OH-PLIF signals increase with an increase in HAB. It is noteworthy that the full sheet (Gaussian) is adopted in **Fig. 14** for visualizing all signals. Moreover, from

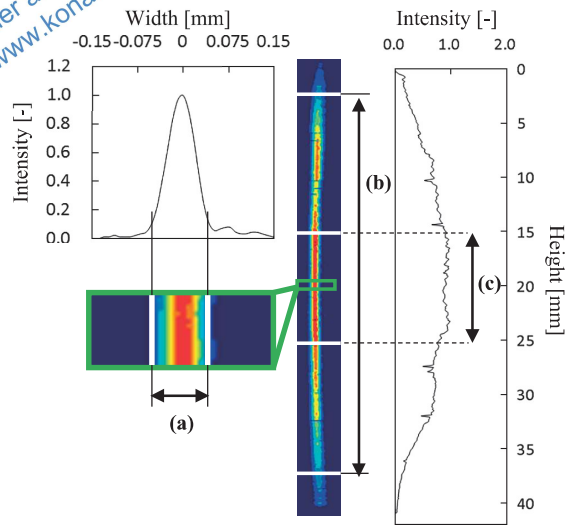

Fig. 12 The laser sheet profile **(a)** width of the laser sheet ($1/e^2$ value) = 0.1 mm, **(b)** height of the Gaussian laser sheet = 29.6 mm, **(c)** height of the homogeneous laser sheet = 10 mm). Reprinted with permission from Ref. (Hayashi J. et al., 2013). Copyright: (2013) Elsevier B.V.

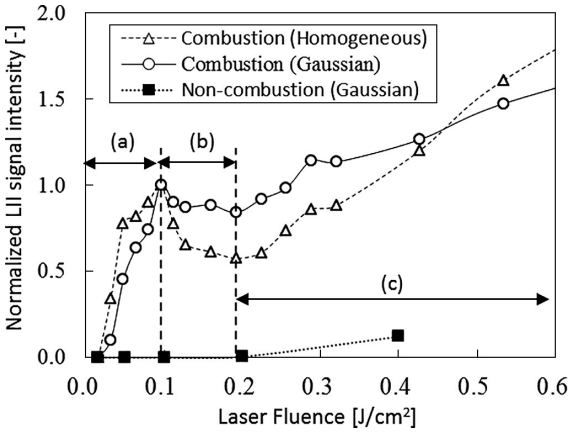

Fig. 13 The LII signal intensity as a function of the laser pulse energy; **(a)** heating up region, **(b)** decreasing region, **(c)** superimposed region. Reprinted with permission from Ref. (Hayashi J. et al., 2013). Copyright: (2013) Elsevier B.V.

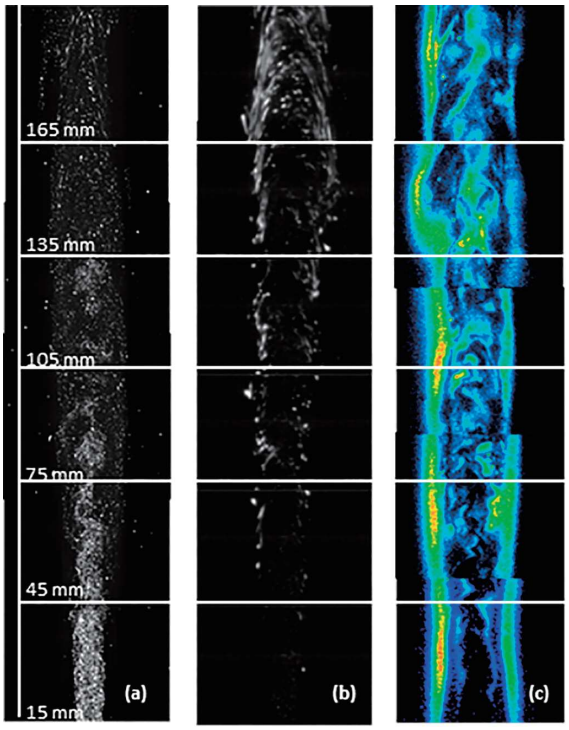

Fig. 14 The instantaneous distributions of **(a)** Mie scattering signals, **(b)** LII signals and **(c)** OH-PLIF signals. Reprinted with permission from Ref. (Hayashi J. et al., 2013). Copyright: (2013) Elsevier B.V.

Fig. 14(b), it is evident that some discrete areas of soot are present near the burner port, the sizes of which increase with an increase in HAB. When the HAB reaches roughly 135 mm from the burner port, the shape of the soot-formation area changes from being discrete to being streaky.

To understand the interaction of coal particles with respect to combustion reaction and soot formation, the averaged radial distributions of the signals of the Mie scattering, the LII and the OH-PLIF at different HABs (60 mm and 120 mm) are shown in **Fig. 15**. The signal intensities of the OH-PLIF and the LII increase with an increase in HAB, as observed in **Fig. 14**. The overlapping region of signals expands with an increase in HAB; this result is due to the turbulent mixing and the expansion of burned gas. Note that the peak value of the OH-PLIF signal, which is formed by the methane pilot flame, appears at the furthest position from the burner center.

Fig. 16 illustrates the radial distributions of gaseous temperatures and oxygen concentrations obtained by using the results of the numerical simulation with TDP model applied to the coal jet burner (Hashimoto N. et al., 2012b), at the same HAB in the experiment. Indeed, the low oxygen concentration region expands in the radial direction with an increase in HAB, which corresponds to the tendency of the LII signal shown in **Fig. 15**. Moreover, from **Fig. 16**, it is evident that the oxygen concentration at the center line of the burner decreases with an increase in HAB. This result suggests that the combustion reaction of volatile matter from pulverized-coal particles consumes the oxygen even in the center of the flame. On the other hand, the LII-signal intensity near the center is low and does not change with an increase in HAB. This is because the temperature at the center of the burner was below 1,500 K, which is not sufficient for soot formation. In fact, the signal intensity of the LII in the high-temperature region (from $r = 5$ to 10 mm) increases with an increase in HAB. In addition, since the signals of the Mie scattering can be found in the same region as the high signal intensity of the LII, a sufficient amount of volatile matter for soot formation is supplied from the pulverized-coal particles in this region. From **Fig. 15**, moreover, it is evident that the signals of the Mie scattering are low in the region around the outer peak of the OH-PLIF signal,

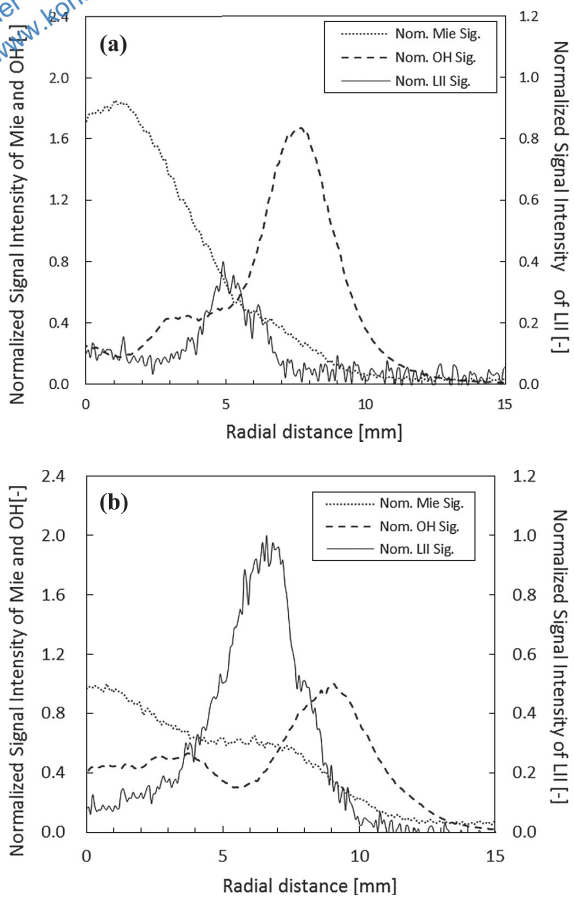

Fig. 15 The ensemble-averaged radial distributions of the Mie scattering signal, LII signal and OH radical chemiluminescence signal normalized by the maximum value at 120 mm; **(a)** $h = 60$ mm, **(b)** $h = 120$ mm. Reprinted with permission from Ref. (Hayashi J. et al., 2013). Copyright: (2013) Elsevier B.V.

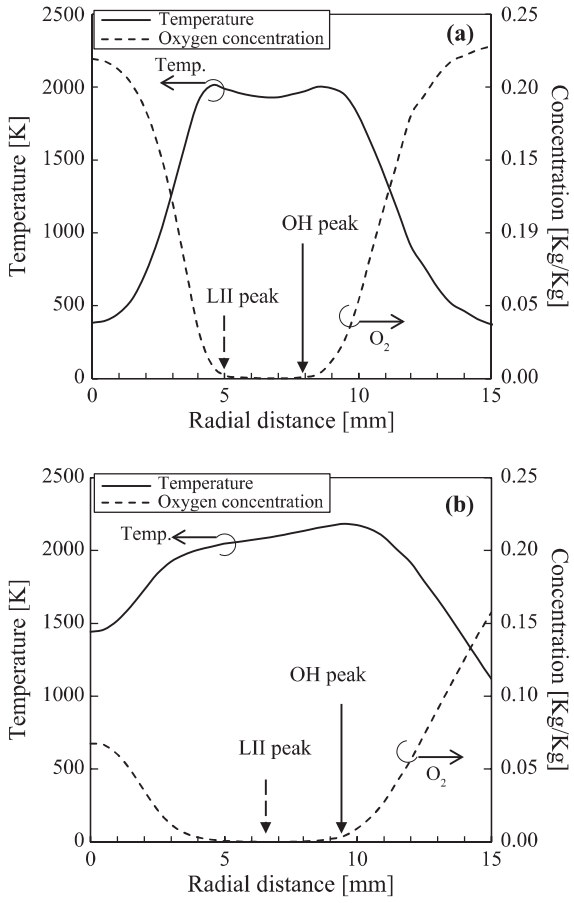

Fig. 16 The radial distribution of temperature and the O_2 concentration (Obtained from Hashimoto et al. 2012b); **(a)** $h = 60$ mm, **(b)** $h = 120$ mm. Reprinted with permission from Ref. (Hayashi J. et al., 2013). Copyright: (2013) Elsevier B.V.

where the gas temperature is high, and the oxygen concentration is minimal. This result means that the required amount of volatile matter for soot formation cannot be formed, because the number density of coal particles is small in this region. Therefore, the signal of LII does not appear in this region in spite of the low oxygen concentration and the high gas temperature.

These results indicate that soot formation is enhanced at locations if the following conditions are satisfied: high gas temperature, low oxygen concentration, and the existence of pulverized-coal particles.

3.4 Primary soot particle distribution measurements in pulverized-coal jet flame

Primary soot-particle size is another important element, with respect to verifying the numerical-simulation models of soot formation for pulverized-coal flames. The spatial distribution of the primary soot particle size was measured employing a combination of a time-resolved LII (TiRe-LII) and the SEM images collected by thermophoretic sampling (TS). **Fig. 17** shows the schematic illustration of TiRe-LII measurement. **Fig. 18** shows the typical SEM images of soot particles collected by TS, the probability-density and the cumulative frequency functions of primary soot-particle size based on sphere equivalent volume of the soot particles (Hashimoto N. et al., 2016a). From **Fig. 18(a-1), (a-2)**, and **(a-3)**, it is clear that the number density of the soot particles on the SEM grid increases with an increase in HAB. This is consistent with the tendency of soot volume fraction measured by the LII as shown in **Fig. 15**.

The red solid circles in **Fig. 18(a-2), (b-2)**, and **(c-2)** represent the cumulative plots of the primary soot-particle sizes, which were calculated by randomly sampling the particles obtained in the SEM images. The approximated cumulative curves of the primary soot-particle sizes are shown as blue solid curves in **Fig. 18(a-2), (b-2)**, and **(c-2)** employing the log-normal function expressed by the following equation:

$$F(D_p) = \frac{1}{2}\mathrm{erfc}\left[-\left(\frac{\ln(D_p) - \ln(D_{p,m})}{\sigma\sqrt{2}}\right)\right] \quad (4)$$

where D_p is the primary soot-particle diameter, and $D_{p,m}$

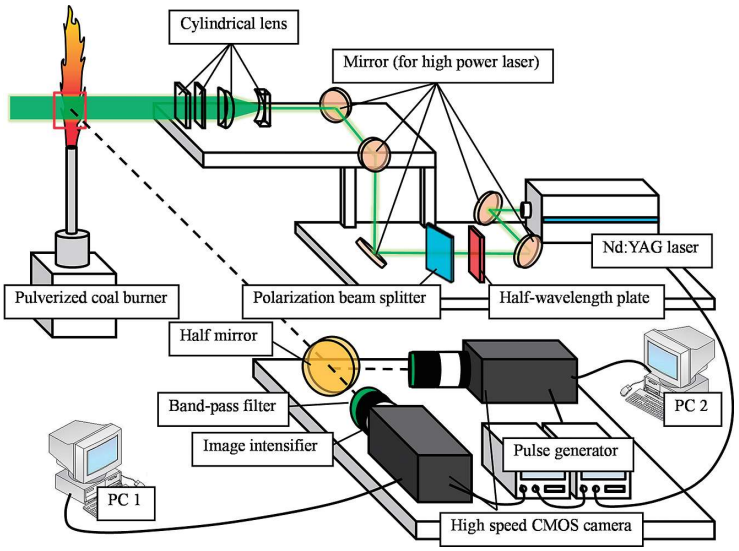

Fig. 17 Schematic of measurement set up for time-resolved laser incandescence (TiRe-LII). Reprinted with permission from Ref. (Hashimoto N. et al., 2016a). Copyright: (2016) Japan Society of Mechanical Engineers.

is the median diameter based on the particle volume. The parameters σ and $D_{p,m}$ are determined by the least-squares method in order to fit the curves to the measured diameter distributions. The green dashed curves indicate the probability density function converted from the blue cumulative frequency curves, which are expressed by the following equation:

$$P(D_p) = \frac{1}{\sqrt{2\pi}\sigma D_p} \exp\left[-\frac{1}{2}\left(\frac{\ln(D_p) - \ln(D_{p,m})}{\sigma}\right)^2\right] \quad (5)$$

Indeed, the primary soot-particle size distribution shifts to the larger side with an increase in HAB. This result indicates that primary soot-particle size increases as said particles move downstream. Moreover, it is also evident that the distribution of the primary soot-particle size widens with an increase in HAB. This result means that the maximum value of the probability density function of primary soot-particle size decreases with an increase in HAB.

Fig. 19 shows the distributions of the primary soot-particle size and the soot-volume fraction. As shown in **Fig. 19**, while the primary soot-particle size increases and the region of soot expands in the radial direction, the radial position of the peak value of the soot-volume fraction does not significantly change with an increase in HAB.

3.5 Simultaneous imaging of Mie scattering, polycyclic aromatic hydrocarbons laser-induced fluorescence, and soot LII with respect to a lab-scale turbulent jet pulverized-coal flame

Since polycyclic aromatic hydrocarbons (PAHs) are known as a soot precursor, information relating to their formation is crucial with respect to the soot-formation processes (Michelsen H.A., 2017 and Desgroux P. et al., 2013). In order to understand the transitional soot formation processes in the pulverized-coal flame, Hayashi et al. (2019) conducted two different simultaneous measurements ("Mie scattering for coal particles with LIF for PAHs" and "LIF for PAHs with LII for soot") in the coal jet burner.

In the following reviewed work, LIF measurement for PAHs using a laser with a wavelength of 355 nm, which is referred to the results reported by Bejaoui S. et al., 2014 and Aizawa T. and Kosaka H., 2008, were conducted. Mie scattering and LII were conducted using the same wavelength as LIF, in order to achieve simultaneous measurements. Laser fluence was set to 0.25 J/cm^2, in order to ensure sufficient signal intensity. Two-dimensional distributions of the signals of Mie scattering, LIF, and LII are shown in **Fig. 20**. The signal intensities of the pulverized-coal particles (Mie scattering), PAHs (LIF signal), and soot particles (LII signal) are represented in green, blue, and red, respectively. Indeed, PAHs exist at the center axis due to the turbulent mixing as shown in **Fig. 20(b)**. This occurs because the PAHs measured according to the LIF are gaseous, and therefore, they follow the gaseous flow. This trend is similar to that of the OH-LIF signal (Hwang S.M. et al., 2005). Conversely, the discrete regions of LII are observed apart from the center line as shown in **Fig. 20(c)**.

The overlaid images of both the Mie scattering and the LIF are shown in **Fig. 21**, from which it is evident that the existing regions of pulverized-coal particles and PAHs slightly overlap. Due to the configuration of this work, the devolatilization tends to begin from the outer side of the main coal/air premixed flow. As a result, a continuous and high-intensity LIF signal can be found in the surrounding area of the Mie-scattering signals. Subsequently, the LIF-signal region expands toward the central region due

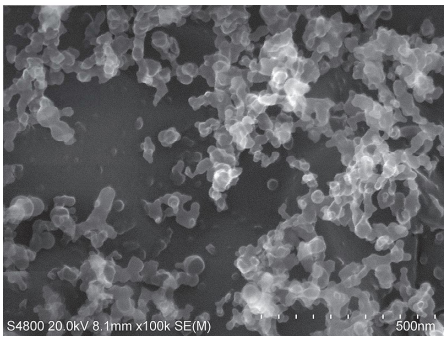

(c-1) Typical image of soot particles sampled at h = 95 mm

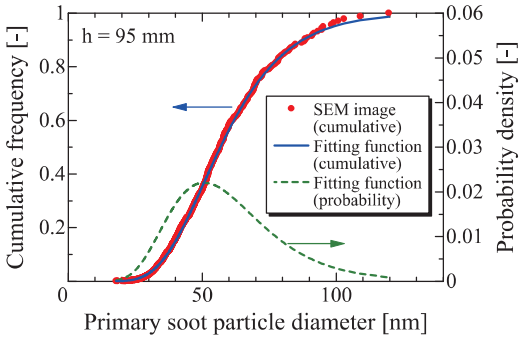

(c-2) Cumulative frequency and probability density functions for primary soot particle diameter (h = 95 mm)

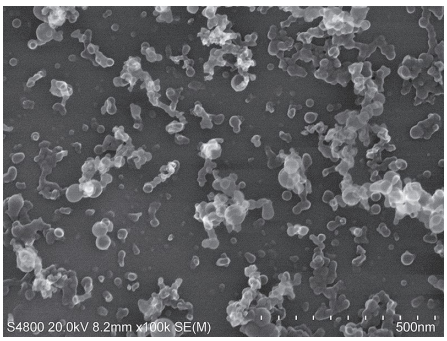

(b-1) Typical image of soot particles sampled at h = 65 mm

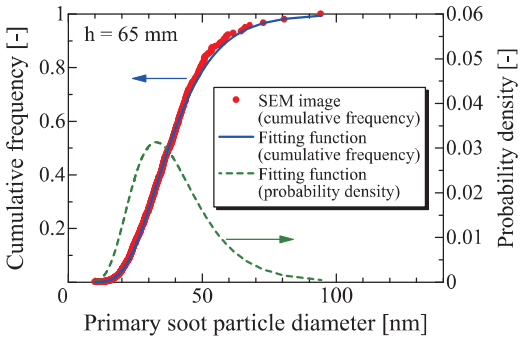

(b-2) Cumulative frequency and probability density functions for primary soot particle diameter (h = 65 mm)

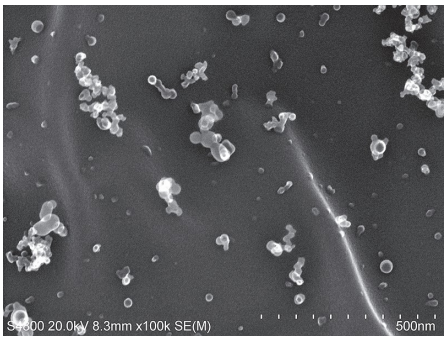

(a-1) Typical image of soot particles sampled at h = 35 mm

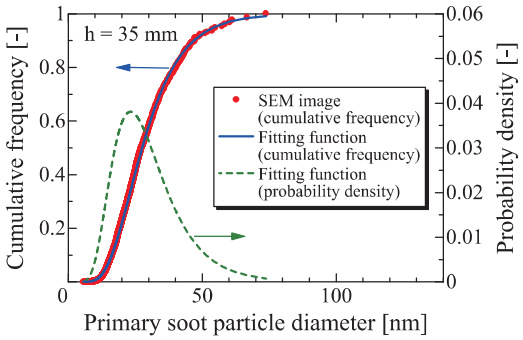

(a-2) Cumulative frequency and probability density functions for primary soot particle diameter (h = 35 mm)

Fig. 18 Typical SEM images of soot particles, probability density and cumulative frequency functions for primary soot particle diameter. Reprinted with permission from Ref. (Hashimoto N. et al., 2016a). Copyright: (2016) Japan Society of Mechanical Engineers.

to the mixing of the surrounding gases. This result is consistent with the numerical results obtained by Hara et al. (2015). Here, it is known that the volatile matter of PAHs with two to three aromatic rings can be formed directly from coal particles (e.g., Zhang L. et al., 2017). This result means that PAHs can exist wherever coal particles exist, so long as the temperature is sufficiently high for devolatilization.

In essence, the existing regions of LIF and LII do not correspond with each other—see **Fig. 21(bottom)**. It is noteworthy that the interference of the LII signal and PAHs-LIF signal cannot be excluded during the scheme of excitation and detection in this work. On the other hand, the LII signal collected at 400 nm with the gate delayed by around 70 ns from the laser incident is unambiguously issued from soot incandescence. The signals of the LII shown in **Fig. 21(bottom)** are well separated from the prompt signal of the LIF. While only a few overlapping locations of LIF and LII are observed, which require careful interpretation, no ambiguity in assigning the prompt signal to the LIF from PAHs exists in any other location. The existing soot region (the regions of LII signal) is limited and discrete at the bottom of the jet flame; moreover, the relative soot-volume fraction increases with an increase in HAB. However, the soot formation was inhibited in the center axis. This occurs because the temperature in this region was relatively low and, moreover, because oxygen was still present at the relevant HAB. Lee S.M. et al. (2004) measured the LIF of PAHs using different wavelengths, showing that the displace-

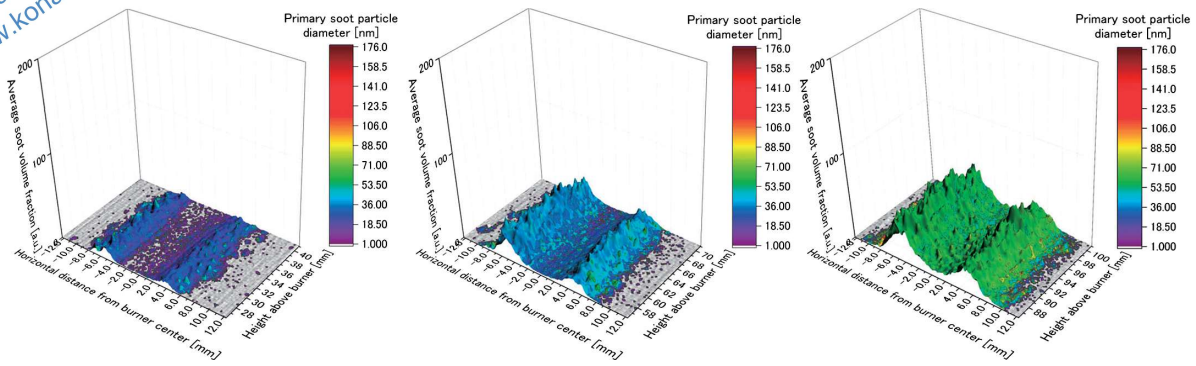

(a) h = 26 - 41 mm **(b)** h = 56 - 71 mm **(c)** h = 86 - 101 mm

Fig. 19 Ensemble-averaged distributions of primary soot particle diameter and soot volume fraction. The color indicates the primary soot particle diameter and the height indicates the soot volume fraction. Reprinted with permission from Ref. (Hashimoto N. et al., 2016a). Copyright: (2016) Japan Society of Mechanical Engineers.

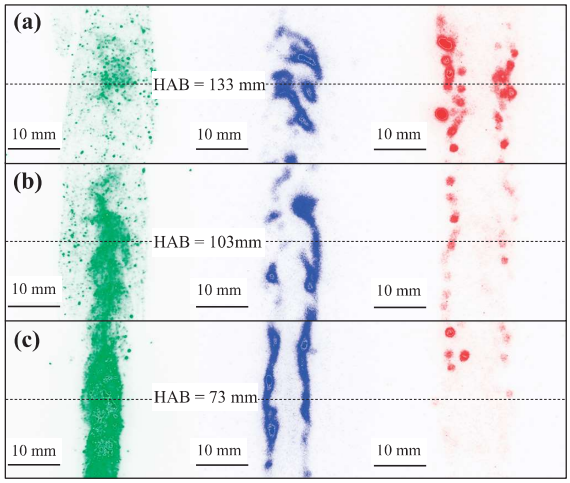

Fig. 20 Two-dimensional distribution of Coal-Mie (in Green), PAHs-LIF (in Blue) and soot-LII (in Red) at different HAB. Reprinted with permission from Ref. (Hayashi J. et al., 2019). Copyright: (2019) Elsevier B.V.

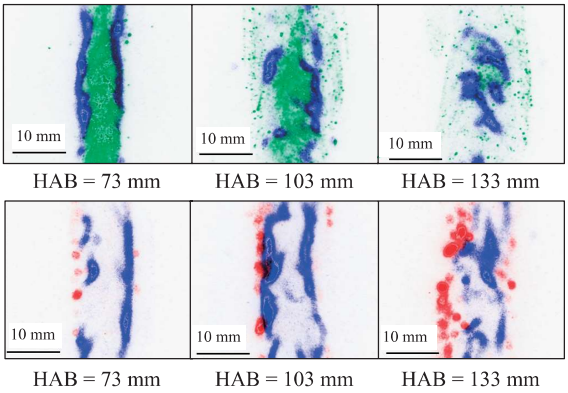

Fig. 21 Overlaid images of Coal-Mie (green) and PAHs-LIF (blue) (top), PAHs-LIF (blue) and soot-LII (red) (bottom) at different HAB. Reprinted with permission from Ref. (Hayashi J. et al., 2019). Copyright: (2019) Elsevier B.V.

ment of both small PAHs and soot is much larger than that of large PAHs. This result suggests that a necessary period of time is required for the development of PAHs to soot, during which time discrete regions form, as shown in **Fig. 21**.

The averaged radial-signal distributions of the Mie scattering, LIF, and LII are shown in **Fig. 22**, from which it is evident that the pulverized-coal particles are spatially distributed and, moreover, that the existing region of them expands with an increase in HAB. The distribution of the LIF signals expands from the fringe to the central axis of coal flame with an increase in HAB; this occurs because the PAHs contained in the volatile matter is evolved from the pulverized-coal particles at high temperatures. Indeed, the signal distribution of LII does not expand from the fringe to the central axis of the coal flame with an increase in HAB.

The volatile-matter mass-fraction distribution for the radial direction at each HAB predicted by the numerical simulation conducted by Hashimoto et al. (2012b) is shown in **Fig. 23**. Indeed, a good correlation between the measured LIF signals (**Fig. 22**) and the predicted volatile-matter mass fraction (**Fig. 23**) exists, even though there are some discrepancies.

3.6 Numerical simulation for soot formation in pulverized-coal combustion fields

Pioneers for the development of soot-formation models for the numerical simulation of coal-combustion fields are Brown A.L. and Fletcher T.H. (1998), who developed a model for RANS-based CFD software. The accuracy of this model was validated using data obtained by TS in a laminar-flow reactor (Ma J. et al., 1996). However, said data were insufficient with respect to validating the accuracy of the model for a turbulent coal combustion field. As mentioned in previous sections, the detailed data including two-dimensional soot-particle volume-fraction distributions in the coal combustion field are now available. Xu K. et al. (2017) developed a soot formation model for RANS-based numerical simulations same as the

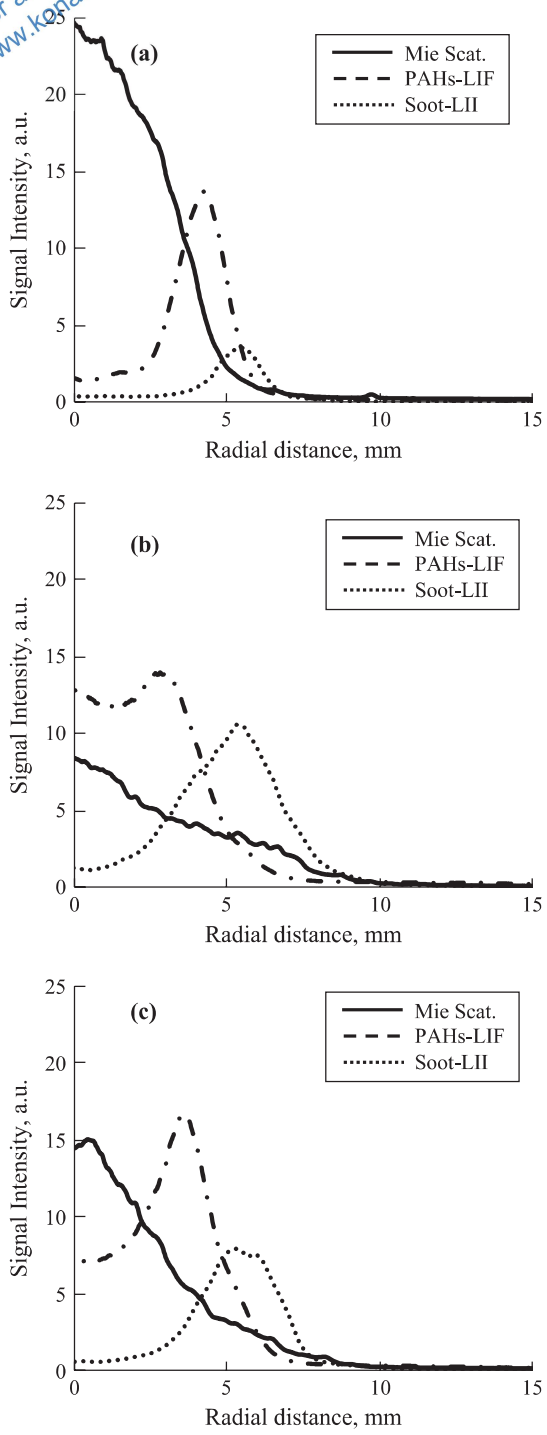

Fig. 22 Radial distributions of Mie Scattering, PAHs-LIF and Soot-LII Reprinted with permission from Ref. (Hayashi J. et al., 2019). Copyright: (2019) Elsevier B.V.

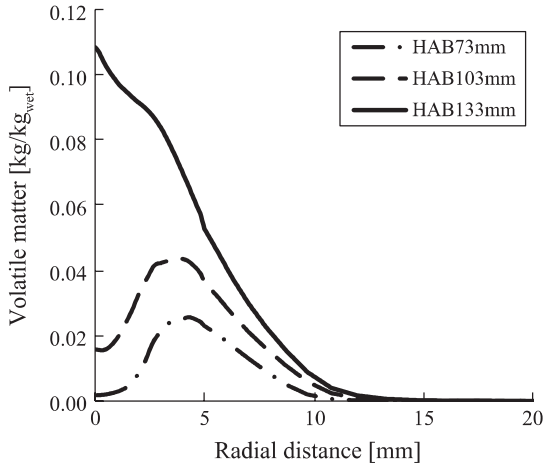

Fig. 23 Radial distributions of volatile matter obtained by Hashimoto N. et al. (2012b). Reprinted with permission from Ref. (Hayashi J. et al., 2019). Copyright: (2019) Elsevier B.V.

model proposed by Brown A.L. and Fletcher T.H. (1998); they validated the simulation using our measured data (Hayashi J. et al., 2013). Muto M. et al. (2018) developed a soot-formation model for the DNS of coal-combustion fields. They used the detailed chemistry for soot formation; their simulation results are yet to be validated. Our research group developed a soot formation model for the LES of coal-combustion fields (Takahashi H. et al., 2019). We combined the soot-formation model proposed by Brown A.L. and Fletcher T.H. (1998) and the TDP model proposed by Hashimoto et al. (2014), because the prediction accuracy of devolatilization strongly affects the soot formation, which is evident in **Fig. 3**.

In the developed model, the parameters V^*, A_v, and E_v are stored in the devolatilization database. The database produced by Hashimoto et al. (2012b) using the FLASHCHAIN model was employed in the study. Since LES is unsteady simulation, the extraction procedure introduced in **Section 2.2**, which was developed for steady-state numerical simulation, was modified so that the TDP model can be applied for LES (Takahashi H. et al., 2019). In the model, four temperatures, which are 500, 800, 1100, and 1400 K, were set to calculate the average particle heating rate for each group of particles with the same initial diameter. The averaged heating rate of 100 particles is compared with particle heating rates in the devolatilization database. Then, the devolatilization parameters associated with a heating rate in the database that is the closest to the averaged particle heating rate calculated from LES is selected are selected as new parameters for the next time step.

In the developed model, soot was treated as a gas phase substance. The conservation equation for soot particles is expressed as follows:

$$\frac{\partial \rho_g \varphi}{\partial t} + \frac{\partial}{\partial x_j}\left(\rho_g u_j \varphi - \rho_g D_s \frac{\partial \varphi}{\partial x_j} - \gamma \frac{\mu}{T}\varphi \frac{\partial T}{\partial x_j}\right) = S_\varphi, \quad (6)$$

where φ is either N_C (soot particle number density) or Y_C (mass fraction of soot). D_s and γ represent the diffusion coefficient for soot particles and the coefficient for the thermophoretic force acting on the soot, respectively. D_s is calculated by the following equation:

$$D_s = \mu / \sigma \rho_g \quad (7)$$

where μ, σ, and ρ_g represent the gas phase viscosity, the Schmidt number (= 700 (Brown A.L. and Fletcher T.H.,

1998)), and the density of the gas phase, respectively. S_{Y_C} (source term of Y_C) is calculated by the following equation:

$$S_{Y_C} = \rho_g \left(\dot{r}_{FC} - \dot{r}_{OC}\right) \tag{8}$$

where $\dot{r}_{FC}$ and $\dot{r}_{OC}$ are the rates of soot formation and oxidation, respectively. S_{N_C} (source term of N_C) is calculated using the following equation:

$$S_{N_C} = \frac{\rho_g}{N_A}\left(\frac{N_A}{M_C \cdot C_{min}} \cdot \dot{r}_{FC} - \dot{r}_{AN}\right) \tag{9}$$

where $\dot{r}_{AN}$, M_C, and C_{min} represent the soot agglomeration rate, the molecular weight of carbon, and the number of carbon atoms per incipient soot-particle, respectively. The term γ in Eq. (6) is the thermophoretic-transport coefficient, which is calculated by the following equation:

$$\gamma = \frac{3}{4\left(1 + \pi \cdot \frac{A}{8}\right)} \tag{10}$$

where A is the accommodation coefficient. The soot formation rate in Eq. (8) is calculated by the following equation:

$$\dot{r}_{FC} = \rho_g \cdot \left(\sum_{i=1}^{4} \frac{Y_{s,Tar_i}}{MW_{Tar_i}}\right) \cdot A_{FC} \cdot e^{-\frac{E_{FC}}{RT}} \tag{11}$$

where MW_{Tar_i}, A_{FC}, E_{FC}, and R represent the molecular weight of the tar species, the pre-exponential factor, the activation energy, and the gas constant, respectively. $Y_{s,\,Tar_i}$ represent the tar-mass fraction, and is obtained from the TDP model. The soot-oxidation rate in Eq. (8) is calculated by the following equation:

$$\dot{r}_{OC} = SA_{v,c} \cdot p_{O_2} \cdot T^{-\frac{1}{2}} \cdot A_{OC} \cdot e^{-\frac{E_{OC}}{RT}} \tag{12}$$

where $SA_{v,C}$ and p_{O_2} represent the soot-particle surface area per unit volume and the partial pressure of oxygen, respectively. The shape of the soot particles is assumed to be a perfect sphere, and $SA_{v,C}$ is calculated by the following equation:

$$SA_{v,C} = (\pi \cdot N_C)^{\frac{1}{3}} \cdot (6 \cdot Y_C)^{\frac{2}{3}} \cdot \rho_g \cdot \rho_C^{-\frac{2}{3}} \tag{13}$$

where ρ_C is the soot particle density (= 1,950 kg/m^3 (Brown A.L. and Fletcher T.H., 1998)). The soot-agglomeration rate in Eq. (9) is calculated by the following equation:

$$\dot{r}_{AN} = 2C_a \left(\frac{6M_C}{\pi \cdot \rho_C}\right)^{\frac{1}{6}} \left(\frac{6\kappa T}{\rho_C}\right)^{\frac{1}{2}} \cdot \left(\frac{\rho_g \cdot Y_C}{M_C}\right)^{\frac{1}{6}} (\rho_g \cdot N_C)^{\frac{11}{6}} \tag{14}$$

where C_a represents the collision frequency constant, which was set as 3 (Brown A.L. and Fletcher T.H., 1998). The values for the pre-exponential factors and the activation energies for $\dot{r}_{FC}$ and $\dot{r}_{OC}$ are listed in **Table 5**.

Radiative heat transfer was calculated using the discrete-ordinate method (Fiveland W.A., 1984) with the S4 approximation. The coal-particle emissivity, ϵ_p, was assumed to be 0.85, according to Kurose et al., 2004. The continuous phase absorption coefficient, k_a, was calculated by the following equation:

Table 5 Pre-exponential factor and activation energy for transport equation source terms. Reprinted with permission from Ref. (Takahashi H. et al., 2019). Copyright: (2019) Elsevier B.V.

Term	Ref.	A	E_v [J/mol]
$\dot{r}_{FC}$	Ma et al., 1996	5.02×10^8 m^3·mol·s	198.9×10^3
$\dot{r}_{OC}$	Lee et al., 1962	1.09×10^4 m^{-1}·s·kg^{-1}·K$^{-1/2}$	164.5×10^3

$$k_a = k_g + k_s \tag{15}$$

where k_g and k_s represent the gas-absorption coefficient and the soot-absorption coefficient, respectively. The value for k_g was set to 0.075, and k_s was estimated by the following equation (Wen Z. et al., 2003):

$$k_s = 1.8644 \times 10^3 f_{v_{soot}} T \tag{16}$$

where $f_{v_{soot}}$ and T represent the soot-volume fraction, and the gas temperature, respectively.

Fig. 24 shows the overview of the computational domain for LES. The entire shape of the domain is a cylinder with a diameter of 200 mm and a length of 560 mm (–60 < HAB < 500 mm). The exit of the burner was set to HAB = 0 mm. The number of nodes was about 1.8 million, and the number of fluid cells was about 2.0 million. The time step of the calculation was set to 2×10^{-5} s.

Fig. 25 shows the comparisons of soot-volume fractions made between the measured and calculated data. In the left-hand side of the figure, the direct photo of the flame and the measured soot volume fraction distribution obtained by LII are shown. The soot-volume fraction was obtained by the ensemble average of 500 shots of the LII signal. Indeed, large soot-volume fractions can be observed at the outer region of the luminous flame. Moreover, from **Fig. 25**, it is evident that the soot-volume fraction increases with an increase in HAB. These tendencies can be reproduced by numerically simulating soot formation, as can be seen in the right-hand side of the figure.

Fig. 26 shows the various comparisons of the radial distributions. The tendency of the signal distributions of Mie scattering to expand radially with an increasing HAB can be reproduced by the calculated distributions of coal-particle surface area in numerical simulation, as shown in **Fig. 26(a)** and **(b)**. In addition, the position of the calculated peak of the soot-volume fraction is almost consistent with the peak of the LII signal. Furthermore, the expansion trends of the soot-volume fraction distributions are evident in both experimental and theoretical results. In **Fig. 26(e)** and **(f)**, it is evident that the conditions of low oxygen concentration, high gas temperature, and

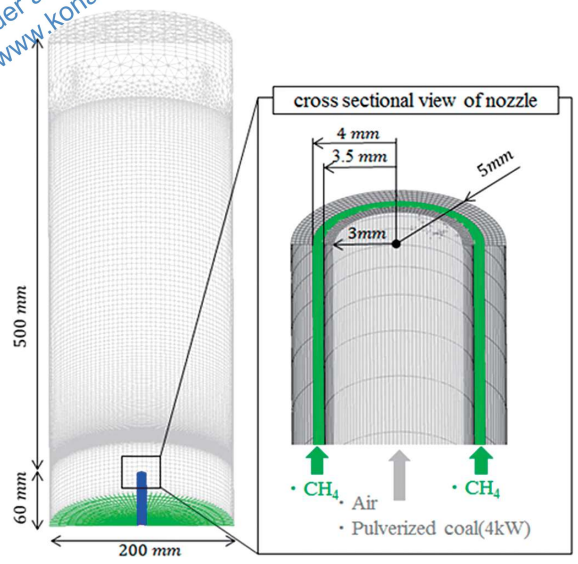

Fig. 24 Computational domain for LES. Reprinted with permission from Ref. (Takahashi H. et al., 2019). Copyright: (2019) Elsevier B.V.

the existence of sufficient pulverized-coal particles are satisfied at the peak position of the soot-volume fraction. This trend can be explained by the following: the peak positions of the net soot-formation rate in **Fig. 26(g)** and **(h)** match the peak positions of the soot-volume fraction in **Fig. 26(e)** and **(f)**. Negative net soot-formation rates are evident at both sides of the base of the soot-volume fraction peak, even though the soot-volume fraction steadily increases at these positions with an increasing HAB. This is because, due to the turbulence mixing effect, the soot particles diffuse from the soot-volume fraction peak toward both sides. Oxygen concentrations where a negative net soot-formation rate is observed are higher than those at the soot-volume fraction peak. This higher oxygen concentration causes a higher rate of soot oxidation. This position results in a significant effect on the formation of a high soot-volume fraction area, even though the absolute value of the net negative formation rate is not significantly high. Basically, the soot particles diffuse from the peak position of the soot-volume fraction; accordingly, in these positions, net soot does not form. This result is the reason why the high soot-volume fraction area is limited to a narrow range of radial distance.

Fig. 27 shows the average gas temperature distributions obtained by LES: **(a)** without soot radiation and **(b)** with soot radiation. From the figure, it is evident that there is the maximum gas-temperature difference of over 100 K between two cases. This temperature difference is caused by the difference in radiation heat flux to surroundings from the coal flame. Average heat flux at the position 100 mm far away from the burner central axis, with soot radiation was 2.95×10^2 W/m^2 while the average heat flux without soot radiation was 2.69×10^{-3} W/m^2. This large difference in heat flux causes significant differences in the predictions of the gas-phase temperatures. Indeed, this

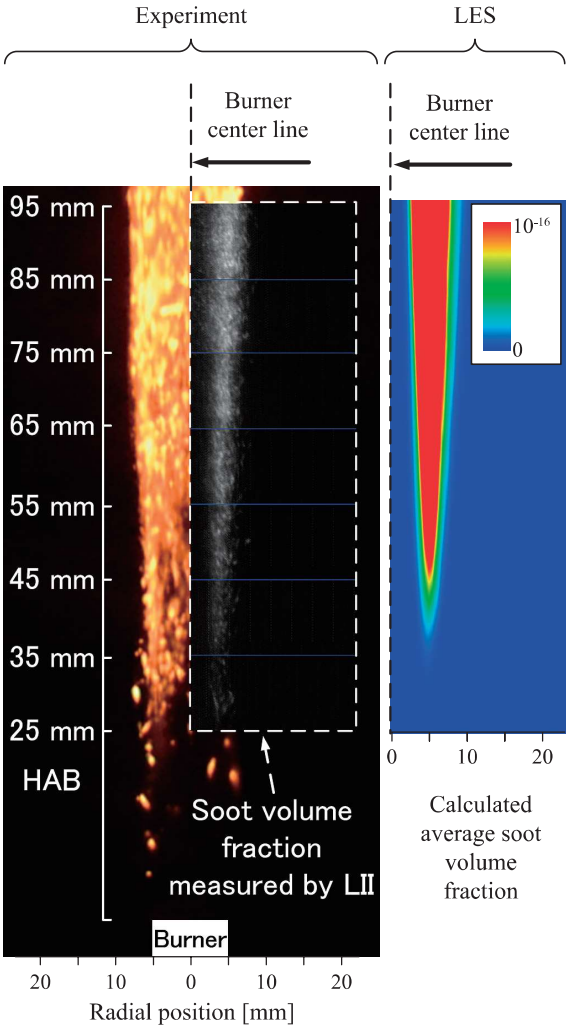

Fig. 25 Comparison between measured (Hashimoto et al., 2016) and calculated soot volume fraction. Reprinted with permission from Ref. (Takahashi H. et al., 2019). Copyright: (2019) Elsevier B.V.

finding indicates the significance of a soot-formation model for numerical simulations of pulverized-coal combustion fields. After all, if a soot formation model is not considered, the gas temperature can be significantly overestimated. Moreover, the accuracy of the gas-temperature predictions significantly influences the majority of processes in coal combustion fields, such as the devolatilization of coal particles, the combustion reaction of volatile matter, char-particle surface reaction, and the formation of pollutants such as NO*x*. Therefore, the soot formation model such as the model in the reviewed study in this paper should be employed for simulations of coal-combustion fields.

4. Prospects for research and development for coal combustion

Although the great efforts for the development of accurate numerical simulation technologies for coal

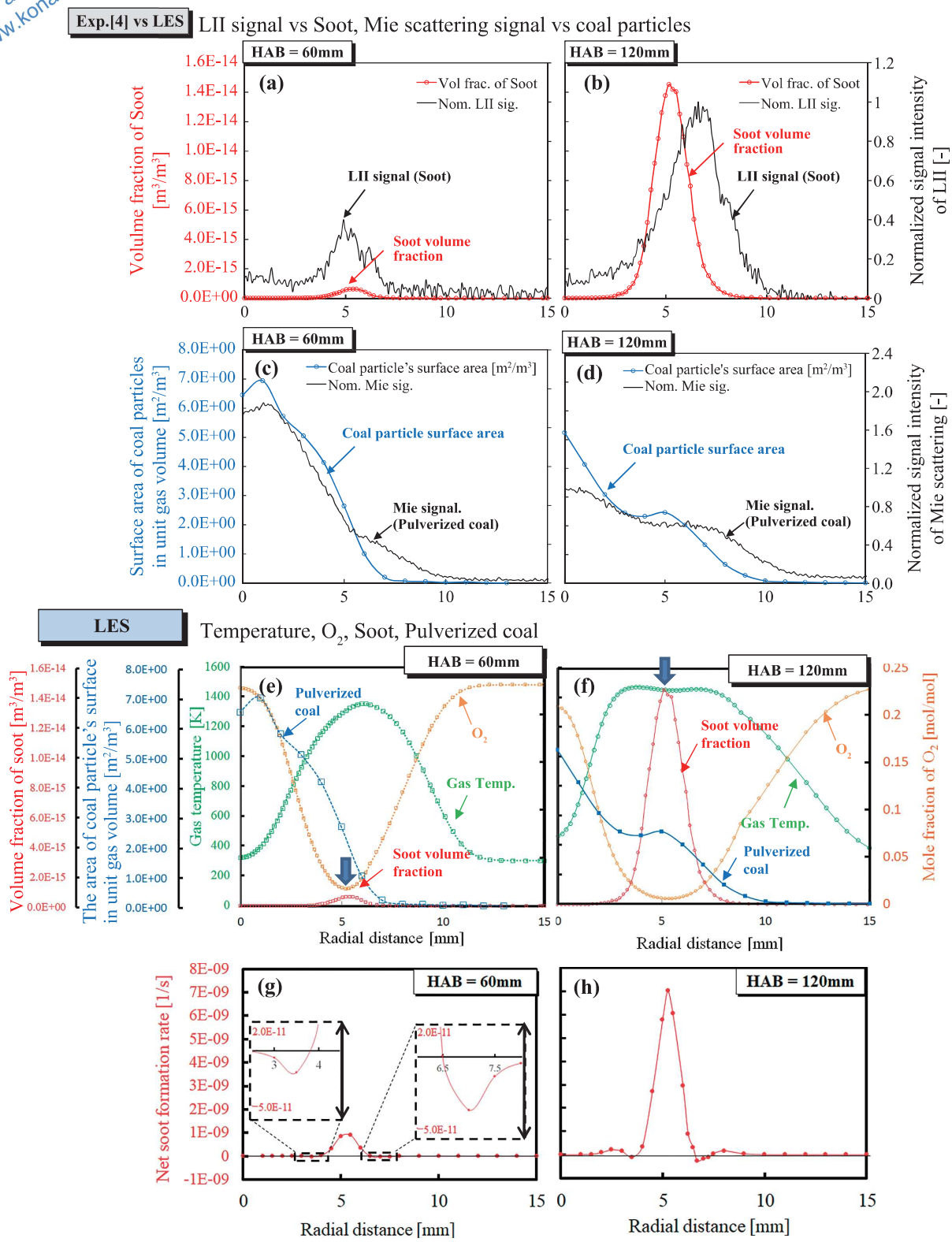

Fig. 26 Comparison of the radial distributions for **(a)**, **(b)** the soot LII signal (Hayashi J. et al., 2013) and the calculated soot volume fraction, **(c)**, **(d)** the Mie scattering signal (Hayashi J. et al., 2019) and the calculated surface area of coal particles, **(e)**, **(f)** the calculated gas temperature and the O_2 concentration, and **(g)**, **(h)** the net soot formation rate at a HAB = 60 and 120 mm, respectively. Reprinted with permission from Ref. (Takahashi H. et al., 2019). Copyright: (2019) Elsevier B.V.

combustion fields have been made by various researchers, there are still a large room for improving the accuracy of the simulation technologies for coal combustion fields. Recently, the flamelet approach, which can treat detailed chemistries with relatively low computational cost by employing the tabulation method, has also been applied for

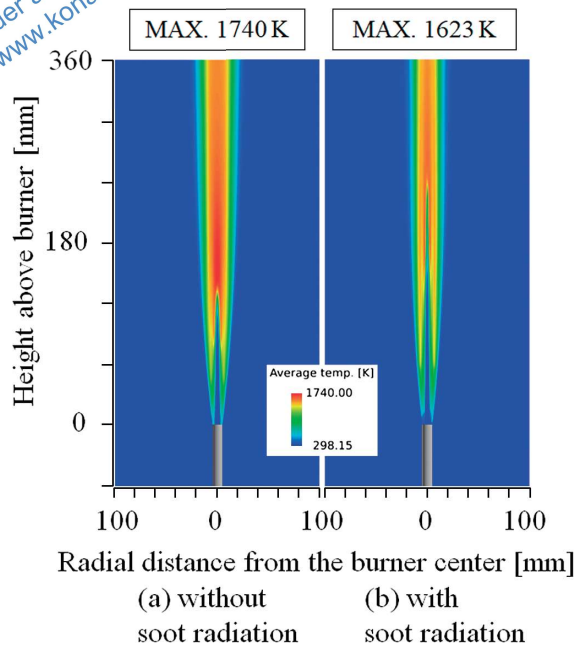

Fig. 27 Effect of soot radiation on the ensemble-averaged gas temperature distribution. Reprinted with permission from Ref. (Takahashi H. et al., 2019). Copyright: (2019) Elsevier B.V.

numerical simulations of coal combustion fields (e.g., Watanabe J. et al., 2017, Wen X. et al., 2019). However, the detailed chemistry for volatile matter combustion has not been developed yet, because detailed molecular for heavy species such as tar cannot be identified due to its complexity. Therefore, the postulated substances such as C_6H_6 are employed as volatile matter, although actual tar species are much heavier species than C_6H_6. Although the methods for flamelet approach have been already developed, the accuracy of numerical simulations cannot be improved until the detailed chemistries for volatile matter and soot particles will be developed. Thus, the clarification of detailed chemistries for volatile matter and soot particles is expected in the future. The accurate prediction technologies for NO*x* emission from coal combustion fields is another important issue. Although the NO*x* emission can be qualitatively predicted by the existing NO*x* models (e.g., Hashimoto N. et al., 2017), developments of more accurate NO*x* formation/reduction models are expected to improve the accuracy of the prediction. The prediction of ash behavior in boilers is also important issue (e.g., Matsui Y. et al. 2019).

In addition to those issues mentioned above, the plants themselves require efficient use; moreover, new types of fuel, such those produced from using renewable energy is expected, because the CO_2 emissions per unit of obtained energy from coal-fired plants are larger than those from other energy plants. One of possible new type fuels for coal-fired boiler is ammonia, which is promising energy carrier in the future. Since ammonia does not have carbon in its molecule, the direct combustion of ammonia can be an option. Many researches have been conducted on the fundamental combustion characteristics of ammonia (Kobayashi et al., 2019, Okafor E.C. et al., 2019, Ichimura R. et al., 2019, Hayakawa A. et al., 2015). Although verification tests and bench-scale tests using large-scale burners have been conducted for the mixed combustion of ammonia and pulverized-coal particles (Kobayashi et al., 2019), research is currently lacking with respect to the fundamental characteristics of mixed combustion of ammonia with pulverized coal particles.

Accordingly, our research group recently started to conduct the fundamental research on the mixed combustion characteristics of ammonia with pulverized coal particle cloud (Hashimoto N. et al, 2019a, 2019b). The flame propagation characteristics of an ammonia-coal particle cloud in turbulent fields has been investigated by using a fan-stirred constant volume vessel (Hadi K. et al., 2019). The developments of the mixing combustion models using the experimental results from these researches for the ammonia-coal particle cloud mixture for numerical simulations is expected in the near future.

5. Conclusions

In this review paper, recent progress of research concerning coal-particle devolatilization model and the soot formation in pulverized coal combustion fields is reviewed. Employing the developed models for coal particle devolatilization and the soot formation can greatly improve the accuracy of numerical simulations for coal combustion fields. The accuracy of the models has been validated by the experimental data measured by various optical diagnostics, such as LDV, LII, TiRe-LII, and LIF. Since non-validated models can cause significant errors in numerical simulations, the use of our measured data by various researchers will be welcomed.

Acknowledgements

Reviewed work in this paper were partly supported by JSPS KAKENHI Grant Number 15637712, MEXT as “Priority issue on Post-K computer” (Accelerated Development of Innovative Clean Energy Systems), JST research promotion program Sakigake (PRESTO) Grant Number JPMJPR1542 and JSPS KAKENHI Grant Number JP19180646.

References

Ahn S., Tanno K., Watanabe H., Numerical analysis of particle dispersion and combustion characteristics on a piloted coax-

ial pulverized coal jet flame, Applied Thermal Engineering, 124 (2017) 1194–1202. DOI: 10.1016/j.applthermaleng.2017.06.103

Aizawa T., Kosaka H., Investigation of early soot formation process in a diesel spray flame via excitation—emission matrix using a multi-wavelength laser source, International Journal of Engine Research, 9 (2008) 79–97. DOI: 10.1243/14680874JER01407

Badzioch S., Hawksley P.G.W., Kinetics of thermal decomposition of pulverized coal particles, Industrial & Engineering Chemistry Process Design and Development, 9 (1970) 521–530. DOI: 10.1021/i260036a005

Bejaoui S., Mercier X., Desgroux P., Therssen E., Laser induced fluorescence spectroscopy of aromatic species produced in atmospheric sooting flames using UV and visible excitation wavelengths, Combustion and Flame, 161 (2014) 2479–2491. DOI: 10.1016/j.combustflame.2014.03.014

Brown A.L., Fletcher T.H., Modeling soot derived from pulverized coal, Energy & Fuels, 12 (1998) 745–757. DOI: 10.1021/ef9702207

Cho C.P., Jo S., Kim H.Y., Yoon S.S., Numerical studies on combustion characteristics of interacting pulverized coal particles at various oxygen concentration, Numerical Heat Transfer, Part A: Applications, 52 (2007) 1101–1122. DOI: 10.1080/10407780701446549

Desgroux P., Mercier X., Thomson K.A., Study of the formation of soot and its precursors in flames using optical diagnostics, Proceedings of the Combustion Institute, 34 (2013) 1713–1738. DOI: 10.1016/j.proci.2012.09.004

Fiveland W.A., Discrete-ordinates solutions of the radiative transport equation for rectangular enclosures, Journal of Heat Transfer, 106 (1984) 699–706. DOI: 10.1115/1.3246741

Fletcher T.H., Kerstein A.R., Pugmire R.J., Grant D.M., Chemical percolation model for devolatilization. 2. Temperature and heating rate effects on product yields, Energy and Fuels, 4 (1990) 54–60. DOI: 10.1021/ef00019a010

Hadi K., Ichimura R., Hashimoto N., Fujita O., Spherical turbulent flame propagation of pulverized coal particle clouds in O_2/N_2 atmospheres, Proceedings of the Combustion Institute, 37 (2019) 2935–2942. DOI: 10.1016/j.proci.2018.09.021

Hara T., Muto M., Kitano T., Kurose R., Komori S., Direct numerical simulation of a pulverized coal jet flame employing a global volatile matter reaction scheme based on detailed reaction mechanism, Combustion and Flame, 162 (2015) 4391–4407. DOI: 10.1016/j.combustflame.2015.07.027

Hashimoto N., Hadi K., Ichimura R., Xia Y., Hashimoto G., Fujita O., Flame propagation characteristics of ammonia and coal particle cloud mixture in turbulent fields: Experimental investigations using a fan stirred constant volume vessel, Sixteenth International Conference on Flow Dynamics, Sendai, Miyagi, Japan, (2019a) OS2-3.

Hashimoto N., Hadi K., Ichimura R., Xia Y., Hashimoto G., Fujita O., Experimental study on turbulent spherical flame propagation characteristics of ammonia / coal particle cloud mixture in a fan-stirred closed vessel, The second Pacific Rim Thermal Engineering Conference, Hawaii, USA, (2019b) PRTEC-24016.

Hashimoto N., Hayashi J., Nakatsuka N., Tainaka K., Umemoto S., Tsuji H., Akamatsu F., Watanabe H., Makino H., Primary soot particle distributions in a combustion field of 4 kW pulverized coal jet burner measured by time resolved laser induced incandescence (TiRe-LII), Journal of Thermal Science and Technology, 11 (2016a) JTST0049. DOI: 10.1299/jtst.2016jtst0049

Hashimoto N., Kurose R., Hwang S.M., Tsuji H., Shirai H., A numerical simulation of pulverized coal combustion employing a tabulated-devolatilization-process model (TDP model), Combustion and Flame, 159 (2012a) 353–366. DOI: 10.1016/j.combustflame.2011.05.024

Hashimoto N., Kurose R., Shirai H., Numerical simulation of pulverized coal jet flame employing the TDP model, Fuel 97 (2012b) 277–287. DOI: 10.1016/j.fuel.2012.03.005

Hashimoto N., Kurose R., Tsuji H., Shirai H., A numerical analysis of pulverized coal combustion in a multi-burner furnace, Energy & Fuels, 21 (2007) 2007. DOI: 10.1021/ef070151o

Hashimoto N., Shirai H., Numerical simulation of subbituminous coal and bituminous coal mixed combustion employing TDP model, Energy, 71 (2014) 399–413. DOI: 10.1016/j.energy.2014.04.091

Hashimoto N., Watanabe H., Numerical analysis on effect of furnace scale on heat transfer mechanism of coal particles in pulverized coal combustion field, Fuel Processing Technology, 145 (2016b) 20–30. DOI: 10.1016/j.fuproc.2016.01.024

Hashimoto N., Watanabe H., Kurose R., Shirai H., Effect of different fuel NO models on the prediction of NO formation/reduction characteristics in a pulverized coal combustion field, Energy, 118 (2017) 47–59. DOI: 10.1016/j.fuproc.2016.01.024

Hayakawa A., Goto T., Mimoto R., Arakawa Y., Kudo T., Kobayashi H., Laminar burning velocity and Markstein length of ammonia/air premixed flames at various pressures, Fuel, 159 (2015) 98–106. DOI: 10.1016/j.fuel.2015.06.070

Hayashi J., Watanabe H., Kurose R., Akamatsu F., Effects of fuel droplet size on soot formation in spray flames formed in a laminar counterflow, Combustion and Flame, 158 (2011) 2559–2568. DOI: 10.1016/j.combustflame.2011.05.015

Hayashi J., Hashimoto N., Nakatsuka N., Tainaka K., Tsuji H., Tanno K., Watanabe H., Makino H., Akamatsu F., Simultaneous imaging of Mie scattering, PAHs laser induced fluorescence and soot laser induced incandescence to a lab-scale turbulent jet pulverized coal flame, Proceedings of the Combustion Institute, 37 (2019) 3045–3052. DOI: 10.1016/j.proci.2018.09.028

Hayashi J., Hashimoto N., Nakatsuka N., Tsuji H., Watanabe H., Makino H., Akamatsu F., Soot formation characteristics in a lab-scale turbulent pulverized coal flame with simultaneous planar measurements of laser induced incandescence of soot and Mie scattering of pulverized coal, Proceedings of the Combustion Institute, 34 (2013) 2435–2443. DOI: 10.1016/j.proci.2012.10.002

Hwang S.M., Kurose R., Akamatsu F., Tsuji H., Makino H., Katsuki M., Application of optical diagnostics techniques to a laboratory-scale turbulent pulverized coal flame, Energy

and Fuels, 19 (2005) 382–392. DOI: 10.1021/ef049867z

Ichimura R., Hadi K., Hashimoto N., Hayakawa A., Kobayashi H., Fujita O., Extinction limits of an ammonia/air flame propagating in a turbulent field, Fuel, 246 (2019) 178–186. DOI: 10.1016/j.fuel.2019.02.110

Johnson G.R., Murdoch P., Williams A., A study of the mechanism of the rapid pyrolysis of single particles of coal, Fuel, 67 (1988) 834–832. DOI: 10.1016/0016-2361(88)90159-7

Kobayashi H., Hayakawa A., Somarathne K.D.K.A., Okafor E.C., Science and technology of ammonia combustion, Proceedings of the Combustion Institute, 37 (2019) 109–133. DOI: 10.1016/j.proci.2018.09.029

Kobayashi H., Howard J.B., Sarofim A.F., Coal devolatilization at high temperatures, Proceedings of the Combustion Institute, 16 (1977) 411–425. DOI: 10.1016/S0082-0784(77)80341-X

Kurose R., Makino H., Large eddy simulation of a solid-fuel jet flame, Combustion and Flame, 135 (2003) 1–16. DOI: 10.1016/S0010-2180(03)00141-X

Kurose R., Makino H., Hashimoto N., Suzuki A., Application of percolation model to particulate matter formation in pressurized coal combustion, Powder Technology, 172 (2007) 50–56. DOI: 10.1016/j.powtec.2006.10.030

Kurose R., Makino H., Suzuki A., Numerical analysis of pulverized coal combustion characteristics using advanced low-NO*x* burner, Fuel, 83 (2004) 693–703. DOI: 10.1016/j.fuel.2003.07.003

Kurose R., Watanabe H., Makino H., Numerical simulations of pulverized coal combustion, KONA Powder and Particle Journal, 27 (2009) 144–156. DOI: 10.14356/kona.2009014

Lee K.B., Thring M.W., Beér J.M., On the rate of combustion of soot in a laminar soot flame, Combustion and Flame, 6 (1962) 137–145. DOI: 10.1016/0010-2180(62)90082-2

Lee S.M., Yoon S.S., Chung S.H., Synergistic effect on soot formation in counterflow diffusion flames of ethylene–propane mixtures with benzene addition, Combustion and Flame, 136 (2004) 493–500. DOI: 10.1016/j.combustflame.2003.12.005

Ma J., Fletcher T.H., Webb B.W., Conversion of coal tar to soot during coal pyrolysis in a post-flame environment, Proceedings of the Combustion Institute, 26 (1996) 3161–3167. DOI: 10.1016/S0082-0784(96)80161-5

Matsui Y., Wakabayashi N., Evaluation of ash melting behavior in pulverized coal-fired furnace from proportion of amorphous phase in fly ash, Fuel, 257 (2019) 116002, DOI: 10.1016/j.fuel.2019.116002

Michelsen H.A., Probing soot formation, chemical and physical evolution, and oxidation: A review of in situ diagnostic techniques and needs, Proceedings of the Combustion Institute, 36 (2017) 717–735. DOI: 10.1016/j.proci.2016.08.027

Muto M., Watanabe H., Kurose R., Komori S., Balusamy S., Hochgreb S., Large-eddy simulation of pulverized coal jet flame–Effect of oxygen concentration on NO*x* formation, Fuel, 142 (2015) 152–163. DOI: 10.1016/j.fuel.2014.10.069

Muto M., Yuasa K., Kurose R., Numerical simulation of soot formation in pulverized coal combustion with detailed chemical reaction mechanism, Advanced Powder Technology, 29 (2018) 1119–1127. DOI: 10.1016/j.apt.2018.02.002

Niksa S., Kerstein A.R., FLASHCHAIN theory for rapid coal devolatilization kinetics. 1. Formulation, Energy & Fuels, 5 (1991) 647–665. DOI: 10.1021/ef00029a006

Okafor E.C., Naito Y., Colson S., Ichikawa A., Kudo T., Hayakawa A., Kobayashi H., Measurement and modelling of the laminar burning velocity of methane-ammonia-air flames at high pressures using a reduced reaction mechanism, Combustion and Flame, 204 (2019) 162–175. DOI: 10.1016/j.combustflame.2019.03.008

Schulz C., Kock B.F., Michelsen H., Will S., Bougie B., Suntz R., Smallwood G., Laser-induced incandescence: recent trends and current questions, Applied Physics B, 83 (2006) 333–354. DOI: 10.1007/s00340-006-2260-8

Solomon P.R., Hamblen D.G., Finding order in coal pyrolysis kinetics, Progress in Energy and Combustion Science, 9 (1983) 323–361. DOI: 10.1016/0360-1285(83)90012-6

Solomon P.R., Hamblen D.G., Carangelo D.G., Serio M.A., Deshpande G.V., General model of coal devolatilization, Energy & Fuels, 2 (1988) 405–420. DOI: 10.1021/ef00010a006

Takahashi H., Hashimoto N., Watanabe H., Kurose R., Fujita O., Soot formation prediction in a pulverized coal combustion field by large eddy simulation with TDP model, Proceedings of the Combustion Institute, 37 (2019) 2883–2891. DOI: 10.1016/j.proci.2018.08.019

Tominaga H., Harada M., Ando T., Suzuki Y., The development of pulverized coal combustion simulator, Journal of NIRE Shigen to kankyo, 6 (1997) 333–343 (in Japanese).

Ubhayakar S.K., Stickler D.B., von Rosenberg C.W., Gannon R.E., Rapid devolatilization of pulverized coal in hot combustion gases, Proceedings of the Combustion Institute, 16 (1976) 427–436. DOI: 10.1016/S0082-0784(77)80342-1

Watanabe H., Kurose R., Komori S., Large-eddy simulation of swirling flows in a pulverized coal combustion furnace with a complex burner, Journal of Environment and Engineering, 4 (2009) 1–11. DOI: 10.1299/jee.4.1

Watanabe J., Okazaki T., Yamamoto K., Kuramashi K., Baba A., Large-eddy simulation of pulverized coal combustion using flamelet model, Proceedings of the Combustion Institute, 36 (2017) 2155–2163. DOI: 10.1016/j.proci.2016.06.031

Wen X., Luo Y., Wang H., Luo K., Jin H., Fan J., A three mixture fraction flamelet model for multi-stream laminar pulverized coal combustion, Proceedings of the Combustion Institute, 37 (2019) 2901–2910, DOI: 10.1016/j.proci.2018.05.147

Wen Z., Yun S., Thomson M.J., Lightstone M.F., Modeling soot formation in turbulent kerosene/air jet diffusion flames, Combustion and Flame, 135 (2003) 323–340. DOI: 10.1016/S0010-2180(03)00179-2

Xu K., Wu Y., Shen H., Zhang Q., Zhang H., Predictions of soot formation and its effect on the flame temperature of a pulverized coal-air turbulent jet, Fuel, 194 (2017) 297–305. DOI: 10.1016/j.fuel.2017.01.032

Zhang L., Qi S-C., Iwanaga K., Uemura K., Zhang L-X., Kudo S., Hayashi J., Furuya K., Norinaga K., An approach for on-line analysis of multi-component volatiles from coal pyrolysis with Li+-attachment ionization mass spectrometry, Fuel Processing Technology, 158 (2017) 141–145. DOI: 10.1016/j.fuproc.2016.12.001

Authors' Short Biographies

Nozomu Hashimoto

Dr. Nozomu Hashimoto is an Associate Professor of Division of Mechanical and Space Engineering, Graduate School of Engineering at Hokkaido University. He received a Ph.D. in Mechanical Engineering from Hokkaido University in 2004. He was previously employed at CRIEPI (Central Research Institute of Electric Power Industry) in Kanagawa, Japan as a Research Associate. His research interests are in multi-phase combustion phenomena such as coal combustion, spray combustion, and flame spread over solid material. Current main subjects are modelling and experiment for coal combustion, droplet evaporation, flame spreading over electric wire, and ammonia flame propagation in turbulent fields.

Jun Hayashi

Dr. Jun Hayashi is an Associate Professor of Department of Energy Conversion Science at Kyoto University and is a Visiting Associate Professor at Osaka University. He received a Ph.D. in Mechanical Engineering from Osaka University. He worked for Osaka University as an Assistant Professor and a Lecturer. His current research interests are in multi-phase combustion phenomena appearing in the industrial combustion facilities including internal combustion engines. His current subjects are a soot formation in the multiphase combustion, a plasma assisted ignition/combustion and a flame structure of hypergolic fuels.